# Large eddy simulation of stably stratified open channel flow

John R. Taylor, Sutanu Sarkar, and Vincenzo Armenio

---

**Articles you may be interested in**

Large eddy simulations of turbulent channel and boundary layer flows at high Reynolds number with mean wall shear stress boundary condition
Phys. Fluids **25**, 110808 (2013); 10.1063/1.4819342

Law of the wall of rotating turbulent shear flow
Phys. Fluids **17**, 098104 (2005); 10.1063/1.2061607

An eddy-viscosity subgrid-scale model for turbulent shear flow: Algebraic theory and applications
Phys. Fluids **16**, 3670 (2004); 10.1063/1.1785131

Anisotropy of turbulence in stably stratified mixing layers
Phys. Fluids **12**, 1343 (2000); 10.1063/1.870386

Length scales of turbulence in stably stratified mixing layers
Phys. Fluids **12**, 1327 (2000); 10.1063/1.870385

---

# Large eddy simulation of stably stratified open channel flow

John R. Taylor and Sutanu Sarkar[a)]
*Department of Mechanical and Aerospace Engineering, University of California San Diego, La Jolla,
California 92037*

Vincenzo Armenio
*Dipartimento di Ingegneria Civile, Universita degli Studi di Trieste, 34127 Trieste, Italy*

Large eddy simulation has been used to study flow in an open channel with stable stratification imposed at the free surface by a constant heat flux and an adiabatic bottom wall. This leads to a stable pycnocline overlying a well-mixed turbulent region near the bottom wall. The results are contrasted with studies in which the bottom heat flux is nonzero, a difference analogous to that between oceanic and atmospheric boundary layers. Increasing the friction Richardson number, a measure of the relative importance of the imposed surface stratification with respect to wall-generated turbulence, leads to a stronger, thicker pycnocline which eventually limits the impact of wall-generated turbulence on the free surface. Increasing stratification also leads to an increase in the pressure-driven mean streamwise velocity and a concomitant decrease in the skin friction coefficient, which is, however, smaller than in the previous channel flow studies where the bottom buoyancy flux was nonzero. It is found that the turbulence in any given region of the flow can be classified into three regimes (unstratified, buoyancy-affected, and buoyancy-dominated) based on the magnitude of the Ozmidov length scale relative to a vertical length characterizing the large scales of turbulence and to the Kolmogorov scale. Since stratification does not strongly influence the near-wall turbulent production in the present configuration, the behavior of the buoyancy flux, turbulent Prandtl number, and mixing efficiency is qualitatively different from that seen in stratified shear layers and in channel flow with fixed temperature walls, and, furthermore, collapse of quantities as a function of gradient Richardson number is not observed. The vertical Froude number is a better measure of stratified turbulence in the upper portion of the channel where buoyancy, by providing a potential energy barrier, primarily affects the transport of turbulent patches generated at the bottom wall. The characteristics of free-surface turbulence including the kinetic energy budget and pressure-strain correlations are examined and found to depend strongly on the surface stratification. © *2005 American Institute of Physics*. [DOI: 10.1063/1.2130747]

## I. INTRODUCTION

Open channel flow is an important model problem with relevance to many environmental and industrial applications. In many cases, temperature gradients are large enough for buoyancy effects to become dynamically important. The present study considers open channel flow with stable stratification imposed by a constant heat flux at the free surface and an adiabatic lower wall. This choice of boundary conditions allows us to contrast the flow behavior when buoyancy effects are present at the turbulence generation site, with the present case where such effects are absent. Specifically, since the near-wall region remains unstratified, the interaction between wall-generated turbulence and an external stable stratification is examined. In addition, the influence of stratification on the well-known characteristics of unstratified turbulence near the free surface is also considered.

Several previous studies have considered stratified channel flow, but in each case stratification was applied with fixed temperature boundaries. Armenio and Sarkar[1] used a large eddy simulation (LES) to study stratified closed channel flow

with a fixed temperature difference $\Delta T$ across the channel. In that study, the authors found that the turbulent momentum and buoyancy fluxes and the turbulent Froude number can be well described as functions of the gradient Richardson number, $\mathrm{Ri}_g$. For large $\Delta T$, they observed a buoyancy-affected region near the walls and a buoyancy-dominated region near the centerline. In contrast, the present study considers open channel flow and a larger Reynolds number, $\mathrm{Re}_\tau = 400$, versus 180, but as will be seen, the largest difference is due to the choice of temperature boundary conditions that qualitatively changes the profile of $N$, the buoyancy frequency.

Komori et al.[2] used steam to heat the surface of water in an inclined open channel at relatively low Reynolds number. Similar to the later results of Armenio and Sarkar,[1] it was found by Komori et al.[2] that $\mathrm{Ri}_g$ governs the effect of buoyancy on the local turbulence. When the fluid became sufficiently stratified, they also observed wavelike motion in the interior accompanied by countergradient heat and momentum fluxes. Although the mathematical representation of the boundary conditions for this experiment is likely to be complicated, it has been argued that they are best approximated by a fixed temperature difference across the channel.[3] Nagaosa and Saito[4] reach similar conclusions from a direct nu-

_____
[a)]Electronic mail: sarkar@ucsd.edu

merical simulation (DNS) of open channel flow with fixed $\Delta T$ across the channel. They considered a friction Reynolds number of 150, a Prandtl number of 1, and friction Richardson numbers of 0, 10, and 20. When the Richardson number is nonzero, turbulence is affected throughout the channel. They also show that stratification reduces the skin friction.

Since all previous studies of open channel flow have considered fixed temperature walls, the near-wall region became stratified, and hence one of the major influences of stratification was a reduction of the near-wall turbulence production. When considering environmental flows, the results of these studies may be analogous to the atmospheric surface boundary layer under conditions of strong surface cooling where a stably stratifying heat flux at the ground can lower turbulent production in the surface layer.[5] In contrast, our proposed boundary conditions are more relevant to the oceanic bottom boundary layer where the bounding surface is adiabatic. See Lien and Sanford[6] for a clear explanation of the differences between atmospheric and oceanic boundary layers.

The choice of the free-surface boundary condition has been shown to be important even when applied to a passive scalar. Handler *et al.*[7] compared the behavior of open channel flow with Neumann and Dirichlet boundary conditions on a passive scalar at the free surface. They found that variations of the surface flux in the Dirichlet case were much larger than variations of surface concentration when a Neumann condition was used. The structure of the scalar field at the free surface was also considerably different between the two cases.

A number of studies have focused on the turbulent statistics and coherent structures at the free surface in unstratified open channel flow. It was originally conjectured that the dynamics of free-surface turbulence would be quasi-two-dimensional. However, Walker *et al.*[8] asserted that turbulence is three-dimensional up to the surface, and even at the surface does not conform to two-dimensional dynamics. In support of this, they demonstrated that vortex stretching is maximal at the free surface, and the tangential vorticity vanishes only in a very thin layer. This conclusion was supported by Nagaosa,[9] who cited the nonvanishing streamwise wall-normal velocity correlation coefficient, $R_{uw}$, as evidence for the three-dimensionality of free-surface turbulence.

The dominant structures at a free surface have been identified as upwellings (fluid impinging on the free surface), downdrafts, and spiral eddies (see Pan and Banerjee[10] and Perot and Moin[11]). Pan and Banerjee[10] demonstrated that the upwellings and downdrafts are driven by active turbulence generated at the bottom of the channel. In numerical simulations at $\mathrm{Re}_\tau = 171$, after allowing the open channel flow to fully develop, they replaced the no-slip bottom wall with a rigid, no-stress surface and observed that the upwellings and downdrafts near the upper free surface quickly decay leaving the surface attached spiral eddies. Since the spiral eddies are predominantly two-dimensional, they suggest that the three-dimensionality and anisotropy observed in free-surface turbulence is caused by impinging patches of three-dimensional turbulence. Calhoun and Street[12] conducted a computational study of turbulence at a free surface with and without density

stratification. They found that with stable stratification, the upwellings seen at the surface are less frequent and weaker relative to an unstratified case.

Two analogies are suggested between the present study and environmental situations. The first is a bottom boundary layer in the deep ocean subject to stable stratification imposed from above. In that problem, as in the present study, a mean flow drives turbulence which creates a well-mixed layer beneath an external stratification. In this analogy, the free surface is an artificial representation of an open boundary. Despite the simplified dynamics considered here compared to an oceanographic setting, we hope to gain fundamental insights into the interaction between wall-generated turbulence and an imposed stable stratification. This should then provide a basis for comparison with studies that include additional physical processes.

The second analogy is an ocean thermocline formed by surface heating in shallow water of nearly uniform depth. In order to eliminate processes beyond the scope of this study, the surface is assumed to be undeformed (the external Froude number is small) and stress-free. Therefore, features common to oceanographic flows such as surface waves, Langmuir cells, and a mixed layer are excluded. The Coriolis parameter is also neglected, corresponding to a large Rossby number valid for the small-scale motions of interest here. It should also be noted that this study does not attempt to model the open ocean thermocline, which may be dominated by large-scale horizontal inhomogeneities and along-isopycnal transport. It is believed that in the open ocean, many of the isopycnals outcrop to the surface (are "ventilated"), where mixing can readily occur via the wind stress.[13] The present study only considers the situation of a heated free surface; radiative and evaporative heat transfer from the ocean to the atmosphere is not accounted for, and therefore the thin thermal sublayer (or "cool skin") where stratification can be unstable[14] is not considered.

The paper is organized as follows. Section II gives the equations to be solved and the corresponding laminar solution. Section III describes the computational method. Section IV describes the results of the simulations with the mean profiles in Sec. IV A, descriptions of various turbulent profiles and free surface effects in Secs. IV B and IV F, and a direct comparison to a previous work by two of the authors in Sec. IV G. Finally, Sec. V contains concluding remarks.

## II. FORMULATION

The geometry of the open channel considered here is shown in Fig. 1. Flow is driven by a uniform pressure gradient aligned with the $x$ axis, and periodicity is applied in both horizontal directions while flat no-slip and no-stress surfaces bound the bottom and top, respectively. The $y$ axis is aligned with the cross-stream direction, and the $z$ axis is normal to the wall. The velocities in the $x$, $y$, and $z$ directions are denoted by $u$, $v$, and $w$. The domain size in the $x$ and $y$ directions is $2\pi h$ and $\pi h$, respectively, where $h$ is the channel depth. The constant, negative density gradient imposed at the free surface can be thought of as surface heating with a constant heat flux if density changes are linearly related to
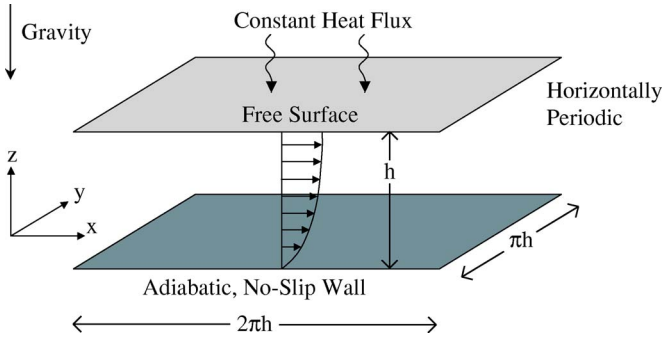
Gravity

Constant Heat Flux

Free Surface

Horizontally Periodic

z

y

x

h

πh

Adiabatic, No-Slip Wall

2πh

FIG. 1. Model domain.

TABLE I. Physical parameters.

| $Ri_\tau$ | $Ri_b \times 10^{-3}$ | $Re_\tau$ | $Re_b$ | Pr |
|-----|-----|-----|-----|-----|
| 0 | 0 | 400 | 6967 | 5 |
| 25 | 1.84 | | 6976 | |
| 100 | 8.80 | | 7002 | |
| 250 | 34.3 | | 7071 | |
| 400 | 76.9 | | 7195 | |
| 500 | 117.8 | | 7310 | |

temperature changes. The total density is given by $\rho_T = \rho_0 + \rho^*(\mathbf{x},t)$, with $\rho^* \ll \rho_0$, allowing the Boussinesq approximation known to be appropriate for stratified water.

## A. Governing equations

The governing equations are nondimensionalized with the channel height $h$, friction velocity $u_\tau = (\tau_w/\rho_0)^{1/2}$, and the absolute value of the imposed free-surface gradient $|\partial \rho^*/\partial z|_s$. The shear stress $\tau_w$ used to define the friction velocity is the horizontally averaged value at the wall which must balance the vertically integrated pressure gradient for steady state ($\Pi h = \langle \tau_w \rangle$). With these choices, the nondimensional governing equations can be written as

$$\frac{D\mathbf{u}}{Dt} = -\nabla p^* + \frac{\nabla^2 \mathbf{u}}{Re_\tau} - Ri_\tau \rho^* \hat{\mathbf{k}} + \Pi \hat{\mathbf{i}}, \qquad (1)$$

$$\frac{D\rho^*}{Dt} = \frac{\nabla^2 \rho^*}{Re_\tau Pr}, \qquad (2)$$

$$\nabla \cdot \mathbf{u} = 0, \qquad (3)$$

$$z = 0: \quad u = v = w = 0, \quad \frac{d\rho^*}{dz} = 0, \qquad (4)$$

$$z = 1: \quad \frac{\partial u}{\partial z} = \frac{\partial v}{\partial z} = w = 0, \quad \frac{d\rho^*}{dz} = -1, \qquad (5)$$

where $\Pi$ is the imposed pressure gradient equal to unity with the present nondimensionalization, $p^*$ is the deviation from the hydrostatic pressure, and the hydrostatic pressure gradient has been canceled with the nominal gravitational force in the usual way. The nondimensional Reynolds, Richardson, and Prandtl numbers are defined as

$$Re_\tau = \frac{u_\tau h}{\nu}, \quad Ri_\tau = -\frac{g}{\rho_0} \frac{\partial \rho^*}{\partial z}\bigg|_s \frac{h^2}{u_\tau^2}, \quad Pr = \frac{\nu}{\kappa}, \qquad (6)$$

where $\kappa$ is the molecular diffusivity. The bulk Richardson number is defined by

$$Ri_b = \frac{\Delta \rho g h}{\rho_0 U_b^2}, \qquad (7)$$

where $U_b$ is the bulk (volume-averaged) velocity through the channel. The parameters used for this study are listed in Table I.

Notice that since the imposed surface density gradient is used to make the density nondimensional, it appears in the Richardson number defined in Eq. (6). This is the only variable quantity in the definition of $Ri_\tau$; since we are considering a fixed forcing pressure gradient $\Pi$, the quantities $\tau_w$ and $u_\tau$ are also fixed. Therefore, increasing $Ri_\tau$ is physically equivalent to increasing the imposed surface stratification. When $Ri_\tau = 0$, density acts as a passive scalar and the velocity field can be checked against previous unstratified open channel studies. When $Ri_\tau > 0$, a negative density gradient is imposed at the free surface, corresponding to stable stratification.

## B. Laminar solution

We will briefly examine the properties of the laminar solution, found by neglecting changes in the horizontal directions, assuming that the velocity profile is independent of time, and solving the nondimensional equations. The laminar velocity is then given by

$$u = \Pi Re_\tau \left( \frac{z^2}{2} - z \right), \quad v, w = 0. \qquad (8)$$

The density profile is unsteady owing to the surface heat flux. The laminar form of Eq. (2) in this flow is

$$\frac{\partial \rho^*}{\partial t} = \frac{1}{Re_\tau Pr} \frac{\partial^2 \rho^*}{\partial z^2}. \qquad (9)$$

The density profile may be divided into the following components:

$$\rho^*(z,t) = f(z) + g(t) + H(z,t), \qquad (10)$$

where $H(z,t)$ is the solution to Eq. (9) with homogeneous (zero gradient) boundary conditions, $g(t)$ is the term owing to surface heating, and $f(z)$ satisfies the inhomogeneous boundary conditions given in Eqs. (4) and (5). The inhomogeneous problem is then

$$g_t = \frac{1}{Re_\tau Pr} f_{zz}, \qquad (11)$$

with

$$f_z(z=1) = \frac{-1}{\mathrm{Re}_\tau \mathrm{Pr}}, \quad f_z(z=0) = 0, \quad g(t=0) = 0, \quad (12)$$

and the homogeneous problem is

$$H_t = \frac{H_{zz}}{\mathrm{Re}_\tau \mathrm{Pr}}, \quad H_z(z=0,1) = 0, \quad H(t=0) = \rho_0(z). \quad (13)$$

Solving Eqs. (11) and (12) first for $f(z)$ and $g(t)$,

$$g(t) = \frac{-t}{\mathrm{Re}_\tau \mathrm{Pr}} \quad (14)$$

and

$$f(z) = \frac{-z^2}{2} + B. \quad (15)$$

Equation (13) is solved using separation of variables with $H(z,t) = \phi(z)\psi(t)$. Using this form and the appropriate boundary conditions gives

$$\psi(t) = e^{-\lambda_n^2 t}, \quad \phi(z) = B_n \cos(\lambda_n z), \quad (16)$$

with

$$\lambda_n = n\pi, \quad n = 0,1,2,3,\dots \quad (17)$$

so the homogeneous solution takes the form

$$H(z,t) = \sum_{n=0}^{\infty} B_n \cos(\lambda_n z) e^{-\lambda_n^2 t}. \quad (18)$$

The constant can be found from the initial condition,

$$\rho^*(t=0) = \rho_0(z) = \frac{-z^2}{2} + \sum_{n=0}^{\infty} B_n \cos(\lambda_n z). \quad (19)$$

Multiplying by $\cos(\lambda_n z)$ and integrating gives

$$B_n = 2 \int_0^1 \left( \rho_0(z) + \frac{z^2}{2} \right) \cos(\lambda_n z) dz. \quad (20)$$

The general laminar solution for the density is then

$$\rho^*(z,t) = \frac{-t}{\mathrm{Re}_\tau \mathrm{Pr}} - \frac{z^2}{2} + \sum_{n=0}^{\infty} B_n e^{-\lambda_n^2 t} \cos(\lambda_n z). \quad (21)$$

Notice that when $t \gg 1$ (and the dimensional time $\gg h/u_\tau$) the last term becomes small compared to the first two when $n \neq 0$. The choice of $B_0 = 0$ is made implying that $\rho^*$ (a negative quantity) is the nondimensional density departure from the value at the bottom wall. Therefore, after sufficient time, there is a linear (in time) heating trend which is *uniform* in space and the solution reduces to

$$\rho^*(z,t) = \frac{-t}{\mathrm{Re}_\tau \mathrm{Pr}} - \frac{z^2}{2}. \quad (22)$$

The value of $\Delta\rho = \rho^*(z=0) - \rho^*(z=1) = 1/2$; i.e., in the laminar case, the dimensional value of the density difference is $|d\rho/dz|_s h/2$ for a given free-surface gradient and channel height.

## C. Density flux balance

In view of the preceding discussion of the laminar density profile, we can separate the unsteady part from the density field as follows. Let

$$\rho^* = \rho_1(t) + \rho(\mathbf{x},t), \quad (23)$$

where $\rho^* = \rho_T(\mathbf{x},t) - \rho_0$, the variable $\rho_1$ denotes the deterministic field that decreases in time owing to the imposed surface heating, and $\rho(\mathbf{x},t)$ is the turbulent density field that is *statistically steady*. Substituting Eq. (23) into Eq. (2) gives

$$\frac{d\rho_1}{dt} + \frac{\partial\rho}{\partial t} = -u_j \frac{\partial\rho}{\partial x_j} + \frac{1}{\mathrm{Re}_\tau \mathrm{Pr}} \frac{\partial^2\rho}{\partial x_j^2}. \quad (24)$$

Taking the Reynolds average of Eq. (24),

$$\frac{d\rho_1}{dt} = -\frac{\partial}{\partial z}\langle\rho'w'\rangle + \frac{1}{\mathrm{Re}_\tau \mathrm{Pr}} \frac{\partial^2\langle\rho\rangle}{\partial z^2}. \quad (25)$$

The right-hand side (rhs) is a function of space only [recall that $\rho(\mathbf{x},t)$ is a statistically steady field] while the left-hand side (lhs) is a function of time only so that, for Eq. (25) to hold, both sides must be constant. In order to evaluate the constant, integrate Eq. (25) from $z=0$ to $z=1$,

$$\int_0^1 \frac{d\rho_1}{dt} dz = \frac{1}{\mathrm{Re}_\tau \mathrm{Pr}} \left[ \left.\frac{\partial\langle\rho\rangle}{\partial z}\right|_{z=1} - \left.\frac{\partial\langle\rho\rangle}{\partial z}\right|_{z=0} \right]. \quad (26)$$

Using the flux boundary conditions, Eqs. (4) and (5), leads to

$$\frac{d\rho_1}{dt} = -\frac{1}{\mathrm{Re}_\tau \mathrm{Pr}}, \quad (27)$$

so

$$\rho_1(t) = -\frac{t}{\mathrm{Re}_\tau \mathrm{Pr}} + C, \quad (28)$$

and the final constant can be absorbed into $\rho_0$. Inserting the expression in Eq. (27) into Eq. (25) and integrating from $z=0$, a useful equation that represents a local balance between turbulent and viscous fluxes is obtained,

$$\mathrm{Re}_\tau \mathrm{Pr}\langle\rho'w'\rangle - \frac{\partial\langle\rho\rangle}{\partial z} = z. \quad (29)$$

We will come back to the interpretation of this equation later. Henceforth we will present results concerning $\rho(\mathbf{x},t)$, the statistically steady turbulent field. After each time integration of Eqs. (1)–(3), the density change owing to $\rho_1(t)$ is subtracted, and the resulting density field becomes statistically steady after an initial transient, at which point statistics are collected.

## III. COMPUTATIONAL METHODS

In order to study the flow in the open channel described above, we use a large eddy simulation (LES). The LES used here is the same as that used by Armenio and Sarkar[1] and the numerical methods are described in detail by Armenio and Piomelli.[15] Since the computational model has already been extensively validated, this is not done here. The filtered equations are integrated using a version of the fractional-step

method of Zang *et al.*,[16] which is second-order accurate in space and time. The spatial derivatives are computed with central finite difference. The convective terms are time-stepped with the Adams-Bashforth scheme, and the diffusive terms are stepped with the implicit Crank-Nicolson scheme. The multigrid method is used to solve the Poisson equation for the pressure.

The subgrid-scale (SGS) stresses are modeled with a dynamic mixed model,

$$\tau_{ij} = \overline{\bar{u}_i \bar{u}_j} - \overline{\bar{u}}_i \overline{\bar{u}}_j - 2C\bar{\Delta}^2 |\overline{S}| \, \overline{S}_{ij}, \qquad (30)$$

where the overbar denotes the filtering operation, $\bar{\Delta}$ is related to the transformation Jacobian $J$ by $\bar{\Delta} = 2J^{-1/3}$, and $S_{ij}$ is the rate of strain tensor. The model coefficient $C$ is determined using a dynamic eddy-viscosity model. The first two terms in Eq. (30) represent the scale-similar part of the model. To model the subgrid density flux, a dynamic eddy diffusivity model is used,

$$\lambda_i = - C_\rho \bar{\Delta}^2 |\overline{S}| \frac{\partial \overline{\rho}}{\partial x_i}, \qquad (31)$$

where the constant $C_\rho$ is evaluated dynamically (see Armenio and Sarkar[1] for more details).

For simplicity, the free surface is assumed to be undeformed, an approximation good for low Froude number. In a DNS of unstratified open channel flow with a deformable free surface, Komori *et al.*[17] found that at $Re_\tau = 160$, the surface is displaced by about 0.01% of the channel depth. Although we are considering a larger Reynolds number, it is expected that any displacements would remain small. Indeed, when $Re_b = 7550$, its maximum value here, the external Froude number,

$$Fr = \frac{U_b}{\sqrt{gh}}, \qquad (32)$$

is less than 0.1 as long as the dimensional channel height is greater than 8.3 cm, which is the case for all applications considered here.

Free-surface flow presents a number of challenges for turbulence modeling. It has been shown that the flow at the free surface is highly anisotropic.[18] Also, as mentioned in the Introduction, Walker *et al.*[8] found that the vertical gradient of the horizontal vorticity vanished only in a very thin layer near the free surface, requiring a fine grid to resolve the mean profile in that region. Shen and Yue[18] show that the energy backscatter (transfer from subgrid scales to larger scales) is maximal at the free surface. It can be expected that these unique factors would make it difficult to apply a generic turbulence model to the free-surface region. Indeed, as shown by Salvetti and Banerjee[19] using DNS data for open channel flow, the dynamic Smagorinsky model performs quite poorly. They find that a dynamic mixed model (the class used here) is a significant improvement, but is not perfect. We attempt to bypass these concerns by using a stretched grid in the vertical with very high resolution at the free surface. As shown in Fig. 2, the vertical grid spacing in the top 20% of the channel is smaller than the Kolmogorov length. It should be noted, however, that even in the upper
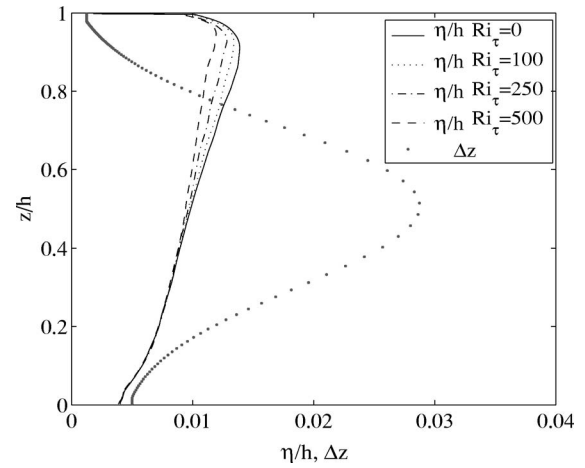


FIG. 2. Kolmogorov scale and vertical grid spacing.

region the model cannot be considered a DNS since the horizontal grid spacing, $\Delta x^+ = 40$ and $\Delta y^+ = 20$, is much larger than the vertical.

Stratification presents another difficulty in numerical modeling since it acts to decrease the vertical length scales of motion, requiring higher resolution. The density microscale[20] is

$$\eta_\rho = \frac{\eta}{\sqrt{Pr}}, \qquad (33)$$

where again $\eta$ is the Kolmogorov length. This scale sets the distance over which density fluctuations can be expected in a turbulent flow and therefore is the limiting resolution for a DNS with $Pr > 1$. Since we are not attempting to fully resolve the diffusive scales of motion, this requirement does not strictly apply here. However, for accuracy of the LES results, the direct effect of stratification on the subgrid scales is limited here by ensuring a sufficiently small grid spacing. The smallest scale at which buoyancy effects are felt is the Ozmidov scale, defined as

$$L_O = \left( \frac{\epsilon}{N^3} \right)^{1/2}, \qquad (34)$$

where $\epsilon$ is the dissipation rate and $N$ is the Brunt-Väisälä (buoyancy) frequency. In all of the cases presented here, the vertical grid spacing is kept smaller than $L_O$, although since they are of the same order near the free surface when $Ri_\tau = 500$, we cannot increase $Ri_\tau$ further with the computational resources available to us.

In order to resolve the details of the turbulence at the free surface, a fine grid must be used in the vertical direction. The grid spacing used here at the top and bottom walls is $\Delta z^+ = 1/2$ and $\Delta z^+ = 2$, respectively. The present numerical method solves the equations with second-order accuracy on a uniform computational grid. In order for the discretization scheme to be second-order accurate on the physical grid, the vertical grid stretching parameter, $r_z$, must obey[21]

$$r_z \equiv \frac{z_{j+1}}{z_j} = 1 + O(\Delta z). \tag{35}$$

The restriction on the grid stretching factor is therefore more stringent at the boundaries where $\Delta z$ is very small. In order to account for this, an exponential function is used to set the vertical grid spacing so that the grid stretching is maximum in the center of the domain where the $\Delta z$ is large. In addition, five uniformly spaced grid points are placed at the lower wall and 16 are placed near the free surface. With these restrictions, more points are needed in the vertical direction, and the grid size is $64 \times 64 \times 128$ in the $x$, $y$, and $z$ directions, respectively. The maximum vertical grid spacing is $\Delta z^+ = 11.5$. In order to ensure that the anisotropy of the grid does not introduce numerical errors, a case with more points in the horizontal was conducted and no significant differences were found.

The bulk Reynolds number after spin-up for each case is listed in Table I, where $Re_b$ is defined as

$$Re_b \equiv \frac{u_b h}{\nu}, \quad u_b \equiv \frac{1}{h}\int_0^h \langle u \rangle dz, \tag{36}$$

and nondimensional time is

$$t_\tau = \frac{t u_\tau}{h}. \tag{37}$$

The case with $Ri_\tau = 0$ is started by interpolating from the velocity and density fields in half of the full-channel simulations of Armenio and Sarkar.[1] The first two stratified cases, $Ri_\tau = 25$ and 100, are both initialized with the $Ri_\tau = 0$ fields at $t_\tau = 4.4$, while the latter two, $Ri_\tau = 250$ and 500, are both initialized with the $Ri_\tau = 100$ data at $t_\tau = 51.8$. Each case has a spin-up period where $Re_b$ increases, indicating that the mean flow initially accelerates owing to an initial imbalance between the wall shear stress, reduced by stratification, and the driving pressure gradient. Eventually all cases tend to an equilibrium where $Re_\tau \simeq 400$, the mean wall shear stress, and $\partial p/\partial x$ are in balance, and $Re_b$ is steady in time. Once a statistically steady state is reached (at $t_\tau \simeq 96.8$ for the $Ri_\tau = 500$ case), each simulation is continued for at least $50 t_\tau$ to obtain a sample size sufficiently large to obtain converged statistics.

## IV. RESULTS

### A. Mean profiles

We begin by describing some mean flow properties. Averages over the horizontal plane and time are denoted by $\langle \cdot \rangle$. The average streamwise velocity profile, nondimensionalized by $u_\tau$, is shown versus $z/h$ in Fig. 3(a). It has already been seen that $u_b$, the bulk-mean velocity, increases with $Ri_\tau$. This increase of $\langle u \rangle$ is seen to occur only in the region near the free surface. Note also that the mean shear in the pycnocline increases with $Ri_\tau$. The spanwise and wall-normal velocities (not shown) are nominally zero. The log-law behavior is shown in Fig. 3(b). A log profile exists in the passive scalar case from $z^+ \simeq 40$ to near the free surface. Increasing $Ri_\tau$ causes the profile to deviate from the log law in the upper
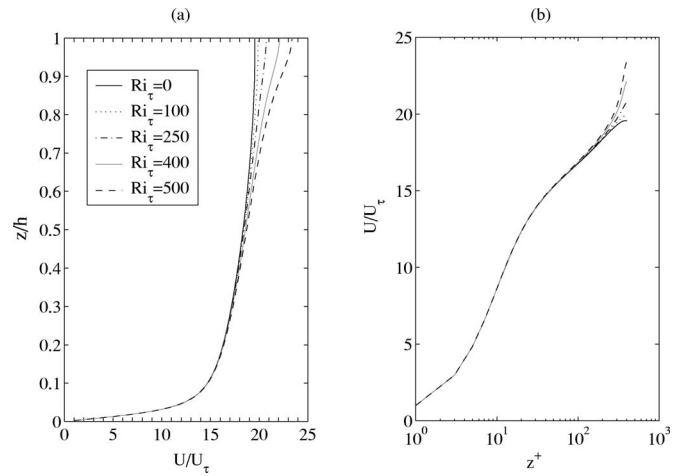


FIG. 3. Mean velocity profiles.

portion of the channel. The location of the deviation from the log-law correlates well with the location where the density gradient begins to diverge from the case of $Ri_\tau = 0$. For example, the location where $\langle u \rangle$ becomes 1% larger than when $Ri_\tau = 0$ is very close to the location where $d\langle \rho \rangle/dz$ is twice the passive scalar value. When $Ri_\tau = 500$ the region of log-law validity is relatively small, approximately 50 wall units.

Nagaosa and Saito[4] also observe an increase in the streamwise velocity when they apply a fixed temperature difference across the channel to produce stable stratification. The region of increased velocity in their case extends from the surface to about 10 wall units from the lower wall, a much thicker region than is seen here. A convenient measure of the bulk change in streamwise velocity is the skin friction coefficient,

$$C_f = 2\tau_w / \rho u_b^2. \tag{38}$$

Table II gives $C_f$ for each case of $Ri_\tau$. For comparison, the values found by Nagaosa and Saito[4] and Armenio and Sarkar[1] are also shown. $Ri_{\tau,\Delta}$ defined with the density difference across the channel,

$$Ri_{\tau,\Delta} = \frac{g h \Delta\rho}{\rho_0 u_\tau^2}, \tag{39}$$

is introduced to measure stratification on a similar basis in all studies. Clearly $C_f$ decreases with $Ri_{\tau,\Delta}$ in all studies, but the dependence observed here is much weaker than the 31% decrease between $Ri_{\tau,\Delta} = 0$ and 20 observed by Nagaosa and Saito[4] and the 22% decrease between $Ri_{\tau,\Delta} = 0$ and 18 observed by Armenio and Sarkar.[1] This can be explained by the relatively limited region affected by stratification in the present study, a qualitative difference with respect to the previous fixed $\Delta T$ cases.

The averaged density profile for each case is plotted as a function of nondimensional height in Fig. 4(a) where the density is made nondimensional by $\Delta\rho$, the difference between wall and surface values as in Komori.[2] The laminar solution, the term $-z^2/2$ in Eq. (22), is also shown. Unlike the gradual variation of $\rho(z)$ in the laminar case, the turbulent flow exhibits a strongly stratified region, or pycnocline, near

TABLE II. Friction coefficient: The present study has an imposed surface heat flux at the upper surface and an adiabatic lower wall. Nagaosa and Saito have an upper free surface and a lower wall, both being isothermal. Armenio and Sarkar have upper and lower walls, both being isothermal.

| Taylor et al. | | | Nagaosa and Saito (Ref. 4) | | Armenio and Sarkar (Ref. 1) | |
|---|---|---|---|---|---|---|
| $Ri_\tau$ | $Ri_{\tau,\Delta}$ | $C_f \times 10^3$ | $Ri_{\tau,\Delta}$ | $C_f \times 10^3$ | $Ri_{\tau,\Delta}$ | $C_f \times 10^3$ |
| 0 | 0 | 6.593 | 0 | 8.71 | 0 | 8.18 |
| 25 | 0.56 | 6.579 | 10 | 7.06 | 18 | 6.37 |
| 100 | 2.7 | 6.535 | 20 | 6.03 | 60 | 4.99 |
| 250 | 10.7 | 6.397 | | | 120 | 3.71 |
| 400 | 24.8 | 6.183 | | | 240 | 3.19 |
| 500 | 39.4 | 5.989 | | | 480 | 240 |

the free surface that overlies a relatively well-mixed region near the lower wall. The presence of the mixed region must depend on the existence of active turbulence since the density gradient of the laminar solution vanishes only near the wall. The thickness of the pycnocline increases with $Ri_\tau$, implying that the turbulence generated near the lower wall is less effective at mixing for large $Ri_\tau$. It should be noted that the density gradient is small but nonzero and nearly constant in the lower portion of the channel and only vanishes in a very thin layer within about five wall units from the wall. Figure 4(b) shows the variation of $\Delta\rho$ between cases. $\Delta\rho$ tends to increase with increasing $Ri_\tau$ (increasing stabilization) but, even for the largest $Ri_\tau = 500$ considered here, $\Delta\rho$ is much smaller than in the laminar case, another indication that the bottom wall continues to strongly generate turbulence.

The scaling of the pycnocline thickness as a function of the imposed stratification can be seen by considering a simple model. From Fig. 4(a) it might be expected that an exponential function will provide a good first-order representation to the density profile. First, for convenience, a nondimensional vertical coordinate is defined from the free surface, $z^* = 1 - z/h$. Then, the density gradient is approximated with an exponential,

$$\frac{d\rho}{dz^*} \simeq A e^{-z^*/L}, \tag{40}$$

with the boundary conditions

$$\frac{d\rho}{dz^*}(z^* = 0) = 1, \quad \frac{d\rho}{dz^*}(z^* \to \infty) = 0. \tag{41}$$

The characteristic length scale of the pycnocline is $L$. Applying the boundary condition at the free surface gives $A = 1$. Figure 5 shows that the density gradient vanishes well before the wall, so the zero flux boundary condition at $z^* = 1$ can be approximated to occur at $z^* \to \infty$, which is satisfied by Eq. (40). Integrating Eq. (40) gives

$$\rho(z^*) - \rho(0) = L(1 - e^{-z^*/L}). \tag{42}$$

Evaluating as $z^* \to \infty$,

$$\rho(\infty) - \rho(0) \simeq \rho(1) - \rho(0) = -\frac{\Delta\rho}{\left.\dfrac{d\rho}{dz}\right|_s h} = L. \tag{43}$$

Therefore, the nondimensional characteristic length of the pycnocline is $L = \Delta\rho/(d\rho/dz|_s h)$. Since $\Delta\rho$ increases with
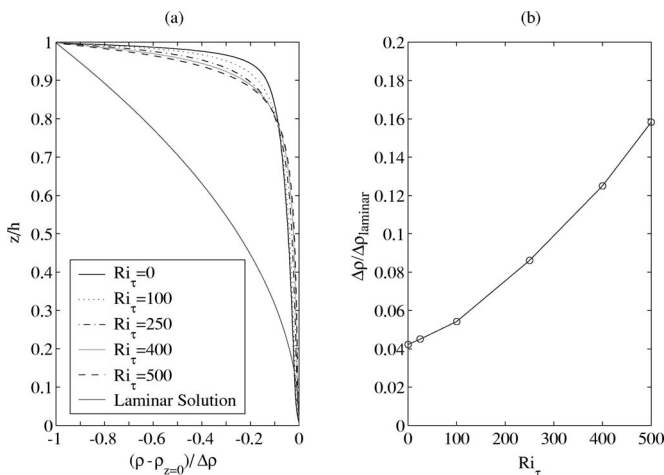


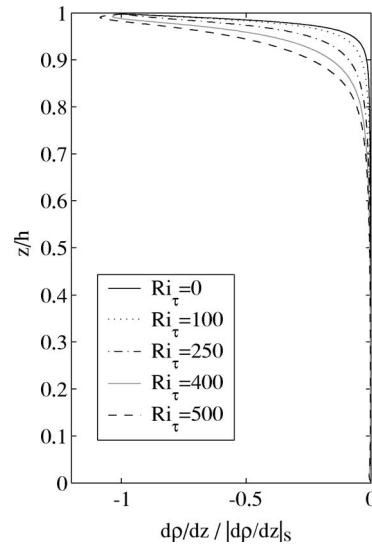FIG. 4. Mean density profiles and density difference across the channel.
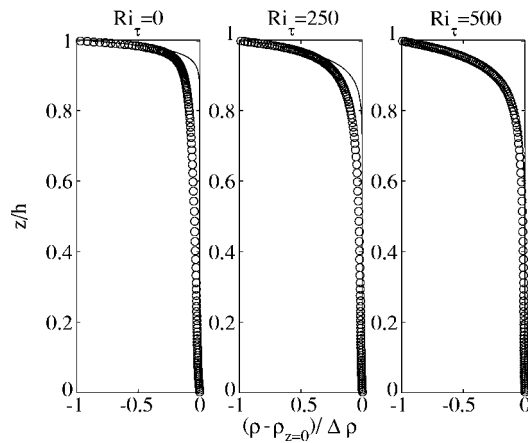


FIG. 5. Mean density gradient.

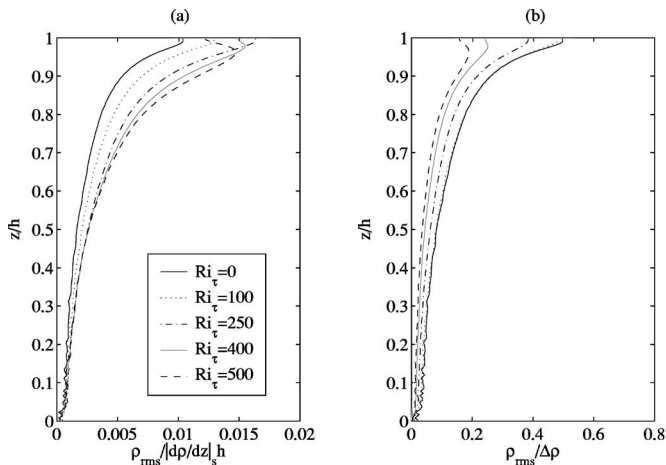FIG. 6. LES data (circles) with an exponential model for the density profiles (lines).



FIG. 7. rms density profiles normalized by (a) free-surface gradient and (b) density jump across channel.
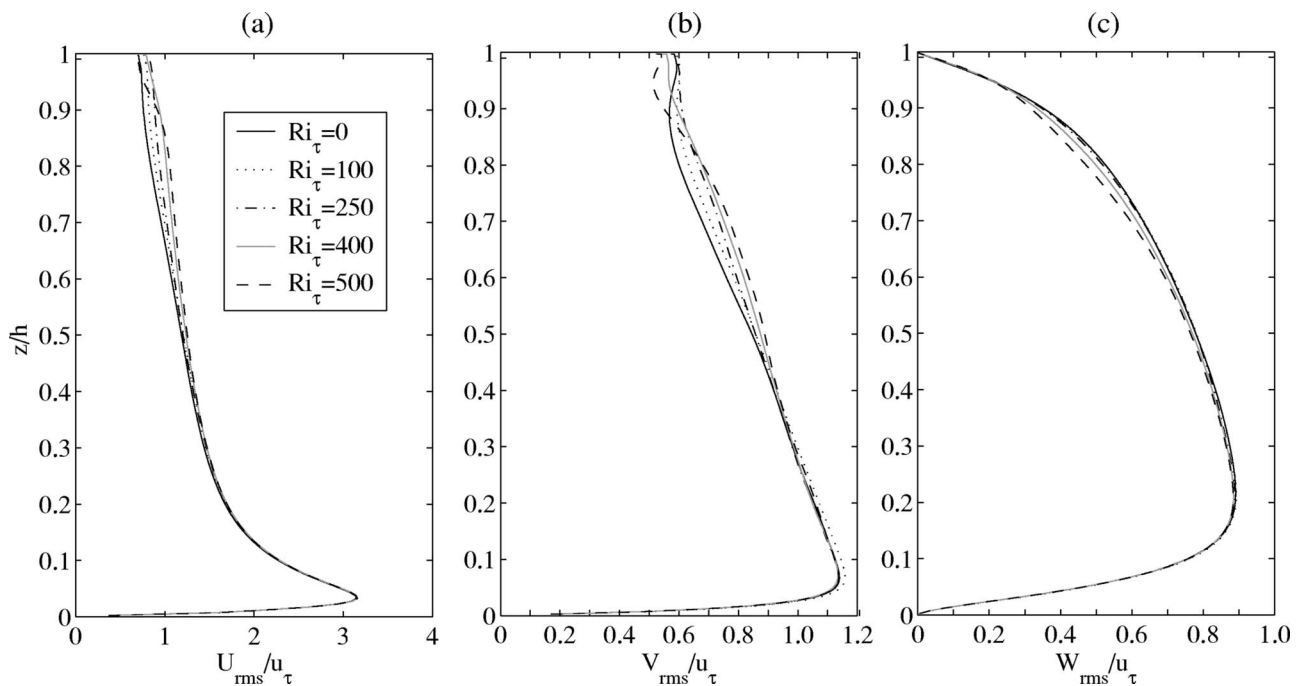
$\mathrm{Ri}_\tau$, the model correctly predicts the same to be true for $L$. The model fit to the density profiles is shown in Fig. 6. The model captures the qualitative behavior of the data, however the decay of $d\rho/dz$ is overestimated for small $\mathrm{Ri}_\tau$.

## B. Turbulence characteristics

Figure 7(a) shows $\rho_{\mathrm{rms}}$ nondimensionalized with the surface gradient and the channel height. In all cases, the maximum occurs in the pycnocline where the density gradient is largest. Nondimensionalized in this way, the magnitude of $\rho_{\mathrm{rms}}$ increases with $\mathrm{Ri}_\tau$, and the location of the maximum is very close to the free surface in all cases but deepens slightly with $\mathrm{Ri}_\tau$. However, from Fig. 7(b), it is apparent that the ratio $\rho_{\mathrm{rms}}/\Delta\rho$ decreases with increasing $\mathrm{Ri}_\tau$, a sign that turbulence is somewhat suppressed by the stable stratification when $\mathrm{Ri}_\tau$ is large.

Figure 8 shows the profile of the rms vertical velocity components. In the lower portion of the channel, the profiles collapse and are consistent with unstratified closed channel flow. In the upper region, $w_{\mathrm{rms}}$ decreases monotonically with increasing $\mathrm{Ri}_\tau$. Since $w_{\mathrm{rms}}$ corresponds to the vertical turbulent kinetic energy, and $\mathrm{Ri}_\tau$ is linked to the size of the buoyancy suppression term in the turbulence kinetic energy (TKE) budget, the observed decrease might be expected. Interestingly, near the free surface where $w_{\mathrm{rms}}$ is suppressed by the geometry in the unstratified case, the dependence on $\mathrm{Ri}_\tau$ is lost. The profiles of $u_{\mathrm{rms}}$ and $v_{\mathrm{rms}}$ are more complicated. In the region between about $0.5 < z/h < 0.85$, the horizontal rms velocity increases with $\mathrm{Ri}_\tau$, consistent with the increase of mean shear in that region. Then, in the near-surface region, the horizontal rms first increases from $\mathrm{Ri}_\tau=0$ to $\mathrm{Ri}_\tau=250$, then decreases sharply in the most stratified cases.

We can begin to trace the cause of the increase in $\langle u \rangle$ with $\mathrm{Ri}_\tau$ by looking at the Reynolds shear stress, $\langle u'w' \rangle$,
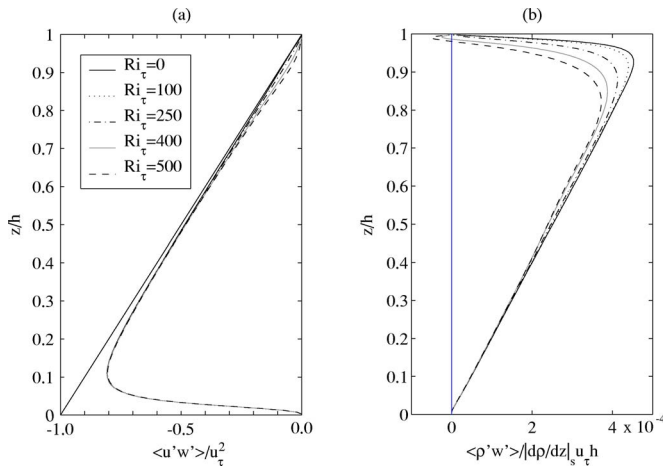


FIG. 8. rms velocity profiles.

FIG. 9. Reynolds shear stress and mass flux.

shown in Fig. 9(a). Also shown is the total shear stress, $\tau(z) = \tau_w(1 - z/h)$. It can be shown (e.g., Pope[22]) that the viscous shear stress is the difference between this line and $\langle u'w' \rangle$. Thus, the increase in the mean vertical shear (equivalently viscous shear stress) in the pycnocline, and therefore $\langle u \rangle$ at the free surface, occurs because of the stratification-induced decrease in the magnitude of $\langle u'w' \rangle$, which is especially strong when $Ri_\tau = 500$. The drop in $\langle u'w' \rangle$ magnitude will be explained using energy arguments in Sec. IV C.

Contributions to the Reynolds stress can be seen by plotting $u'$ vs $w'$ as shown in Fig. 10 for $z/h = 0.84$. In each quadrant of the plots is a label showing its contribution to $\langle u'w' \rangle / u_\tau^2$. The upwelling events can be clearly seen for $Ri_\tau = 0$ by an anisotropic tail extending to the upper left. When $Ri_\tau = 500$, the strength of the upwellings is diminished, and the distribution becomes more isotropic. In both cases, downwelling events are not as energetic as upwelling bursts, and contribute less to $\langle u'w' \rangle$.

The buoyancy flux, $B = -g/\rho_0 \langle \rho'w' \rangle$, couples the vertical component of turbulent kinetic energy and the turbulent potential energy. Figure 9(b) shows the mass flux, $\langle \rho'w' \rangle$, nondimensionalized by the free-surface density gradient, the channel height, and $u_\tau$. Vertical motion under the negative mean density gradient implies a positive mass flux (negative buoyancy flux) for the usual case of cogradient transport. The mass flux decreases everywhere with increasing $Ri_\tau$ and has a small countergradient value near the surface when $Ri_\tau = 500$. Countergradient transport is associated with falling
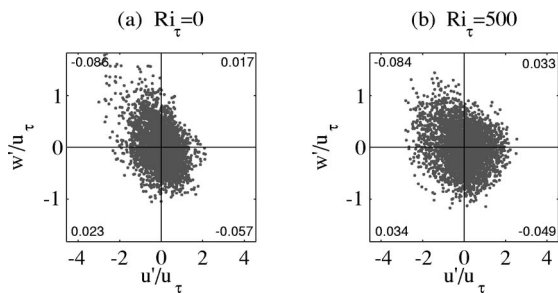
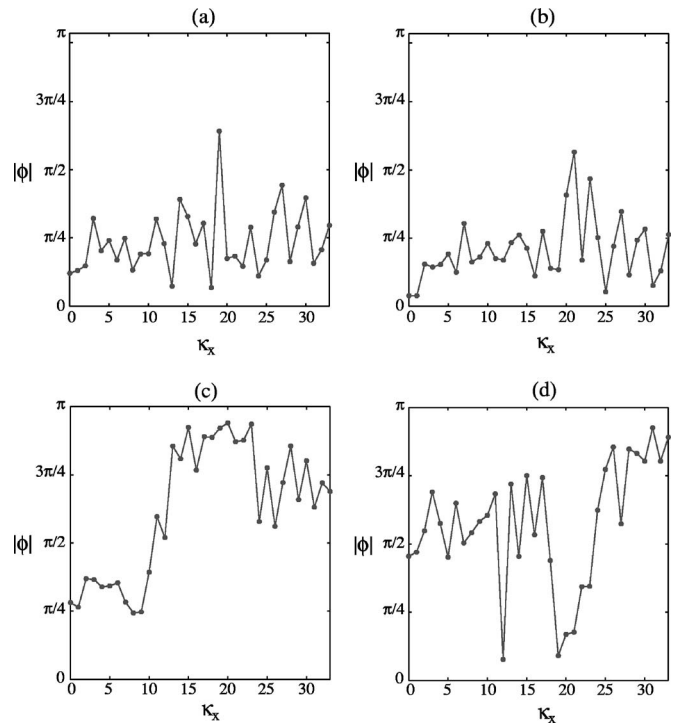

FIG. 10. $u'$ vs $w'$ at $z/h = 0.84$.



FIG. 11. Absolute value of the velocity-density phase angle. (a) $Ri_\tau = 0$, $z/h = 0.927$, where $\langle \rho'w' \rangle$ is maximum; (b) $Ri_\tau = 0$, $z/h = 0.99$ near the free surface; (c) $Ri_\tau = 500$, $z/h = 0.825$, where $\langle \rho'w' \rangle$ is maximum; (d) $Ri_\tau = 500$, $z/h = 0.99$, where $\langle \rho'w' \rangle$ is minimum and negative.

heavy fluid that releases potential energy to kinetic energy. Komori et al.[2] also find a countergradient heat flux, although they report it being much larger and appearing at lower $Ri_g$ than in the present simulations. The difference is presumably due to the boundary conditions, since in the Komori et al.[2] experiments, the wall and free surface were roughly held at fixed temperature. Large countergradient buoyancy fluxes were also seen in the study by Armenio and Sarkar[1] in a closed channel with fixed temperature boundary conditions at the walls.

The source of the countergradient buoyancy flux can be seen by examining the phase angle of the velocity-density spectra. By defining the cospectrum, $Co_{\rho w}(\kappa_x, z)$, and quadrature spectrum, $Qu_{\rho w}(\kappa_x, z)$, as the real and imaginary parts, respectively, of

$$\sum_{\kappa_y} \hat{w}(\kappa_x, \kappa_y, z)\hat{\rho}^*(\kappa_x, \kappa_y, z), \tag{44}$$

the phase angle $\phi(\kappa_x, z)$ can be defined by

$$\tan(\phi) = \frac{Qu_{\rho w}}{Co_{\rho w}}. \tag{45}$$

The absolute value of the phase angle is shown for $Ri_\tau = 0$ and $Ri_\tau = 500$ in Fig. 11. The phase angle is averaged over data at several time instants and linearly weighted by the absolute value of the energy at the corresponding $\kappa_x$ and $t$,
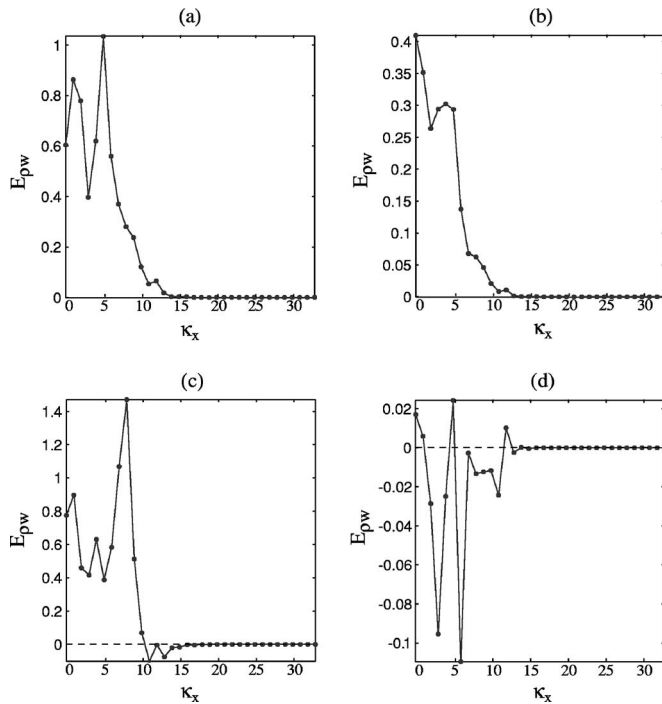
FIG. 12. Energy of the velocity-density cospectrum at (a) $Ri_\tau=0$, $z/h=0.927$; (b) $Ri_\tau=0$, $z/h=0.99$; (c) $Ri_\tau=500$, $z/h=0.825$; and (d) $Ri_\tau=500$, $z/h=0.99$.



FIG. 13. Normalized eddy viscosity and eddy diffusivity.

$$E_{\rho w}(\kappa_x,z,t) = \sum_{\kappa_y} (\hat{\rho}\hat{w}^* + \hat{\rho}^*\hat{w}), \qquad (46)$$

which is shown in Fig. 12. When $0 \leq |\phi| < \pi/2$, the flow acts to mix the density field, $\langle\rho'w'\rangle$ is positive, and energy is extracted from the turbulent kinetic energy by buoyancy. When $\pi/2 < |\phi| \leq \pi$, the value of $\langle\rho'w'\rangle$ is negative, and buoyancy is a source of turbulent kinetic energy since, on average, heavy fluid is falling and light fluid is rising. It is known that linear internal waves are associated with a phase angle $|\phi| = \pi/2$, see, e.g., Gill.[23] The horizontal wave number $\kappa_x$ in Fig. 11 has been nondimensionalized by the channel height. For all cases, most of the energy is contained in wave numbers $\kappa_x < 15$ as seen in Fig. 12. Figures 11(a) and 11(b) show that when $Ri_\tau=0$, all wave numbers are in the range of active mixing as would be expected for a passive scalar. When $Ri_\tau=500$, and at the location of maximum buoyancy flux, $z/h=0.825$ [see Fig. 11(c)], the large energy-containing scales have $|\phi| < \pi/2$, indicating mixing, while the small scales exhibit a countergradient buoyancy flux of small magnitude, see Fig. 12(c). Near the free surface where the buoyancy flux is minimum and negative, most of the energy-containing scales appear to be associated with linear internal waves ($|\phi| \simeq \pi/2$) or mild countergradient fluxes, while the small scales are more strongly countergradient but of small magnitude. From Fig. 12(d) it can be seen that the dominant contribution to the countergradient buoyancy flux comes generally from the large scales of motion.

Although the influence of $Ri_\tau$ on the bulk Reynolds stress is rather small as also reflected in small changes to the friction 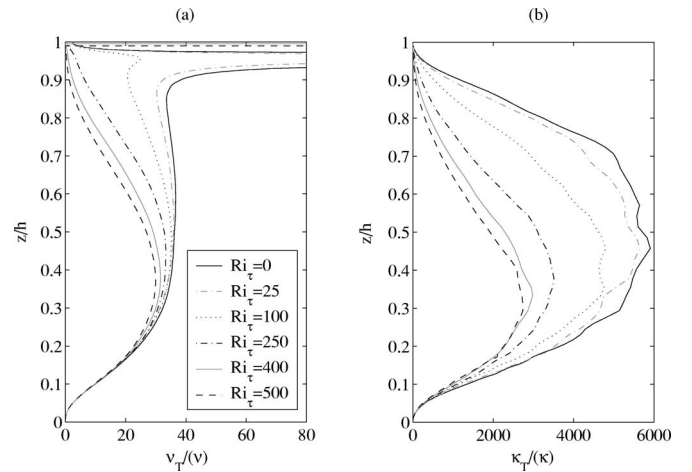coefficient, the *local* turbulent diffusion is strongly affected in a significant portion of the channel, as can be seen by defining the eddy viscosity, $\nu_T$,

$$-\langle u'w'\rangle = \nu_T \frac{d\langle u\rangle}{dz}. \qquad (47)$$

The mean streamwise stress balance can then be written

$$\tau_w\left(1 - \frac{z}{h}\right) = \frac{d\langle u\rangle}{dz}\left(\frac{1}{Re_\tau} + \nu_T\right), \qquad (48)$$

so any change in the mean shear between cases must also be reflected in the eddy viscosity, plotted in Fig. 13(a). Eddy viscosity decreases very significantly with $Ri_\tau$, even in the interior of the open channel where stratification is relatively low. The mass diffusivity $\kappa_T$, defined as

$$\langle w'\rho'\rangle = -\kappa_T \frac{d\langle\rho\rangle}{dz}, \qquad (49)$$

also decreases very significantly with $Ri_\tau$ at nearly every vertical level as shown in Fig. 13(b).

The buoyancy or Brunt-Väisälä frequency, $N$ defined as

$$N^2 = \frac{-g}{\rho_0}\frac{\partial\langle\rho\rangle}{\partial z}, \qquad (50)$$

is shown in the left panel of Fig. 14. This plot makes clear the deepening and strengthening of the pycnocline with increasing $Ri_\tau$. A local measure of the relative importance of stratification and shear, the gradient Richardson number can be defined using $N$ and the mean shear, $S=d\langle u\rangle/dz$, so that $Ri_g=N^2/S^2$, also shown in Fig. 14. The gradient Richardson number measures the relative importance of turbulent production by the mean shear, and suppression by the stable stratification. As such, it is associated with the stability of the flow, with linear instability possible only if $Ri_g<1/4$ somewhere in the domain. Since $N$ increases with $Ri_\tau$, it is surprising that above the linear stability threshold, $Ri_g$ tends to decrease with $Ri_\tau$. Evidently an increase in mean shear more than compensates for the increase in $N$.
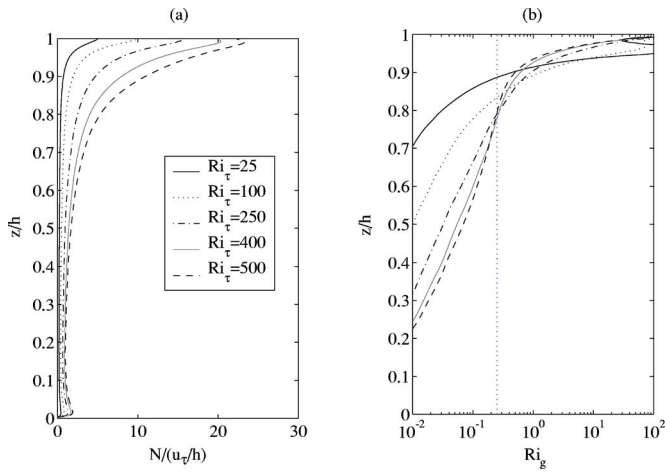
FIG. 14. Brunt-Väisälä frequency and gradient Richardson number.



FIG. 15. Ratio of potential energy needed to reach the upper surface from a given location to the vertical TKE at that location.

## C. Turbulence-surface interactions

The increase in $\langle u \rangle$ seen near the free surface in the highly stratified cases can be attributed to a potential energy barrier created by the presence of the pycnocline. It has been shown previously[10] that a large portion of the Reynolds stress near an unstratified free surface in open channel flow is due to impinging of low-speed fluid advected from the near-wall region. While the wall-generated low speed streaks do not maintain coherence over distances comparable to the channel height in this study, low-speed ejections from the wall boundary layer are observed to directly impact the free surface in the low stratification cases.

That the upward advection of low speed fluid to the surface is inhibited for large $Ri_\tau$ is implied by the drop in correlation between $u'$ and $w'$ in the Reynolds stress of Fig. 9(b). To determine the fate of turbulence generated near the lower wall more directly, it is useful to consider an energy balance. Traditionally, the buoyancy scale $w_{rms}/N$ gives a measure of how far a fluid parcel would travel vertically if all of its vertical turbulent kinetic energy were converted to potential energy. For the situation considered here, this is not accurate since $N$ is highly variable in the vertical direction. For instance, in the highly active region near the lower wall, $w_{rms}$ is large while $N$ is small, so the buoyancy scale may be very large. However, the presence of a strong pycnocline near the surface adds to the potential energy barrier, and may prevent direct interaction with the surface.

As a more accurate measure of the ability of local turbulence to reach the free surface, we compare the vertical turbulent kinetic energy to the potential energy deficit relative to the free surface. This ratio, shown in Fig. 15, is

$$\frac{g \int_z^h [\langle \rho \rangle(z) - \langle \rho \rangle(z')] dz'}{\frac{1}{2}\langle w'w' \rangle}. \qquad (51)$$

As expected, this ratio is largest when $Ri_\tau=500$ since this case has a stronger, deeper pycnocline, requiring more energy to reach the free surface. The cases with the lowest stratification, namely $Ri_\tau=25$ and $Ri_\tau=100$, have small values of this ratio. Since the pycnocline is weak in relation to
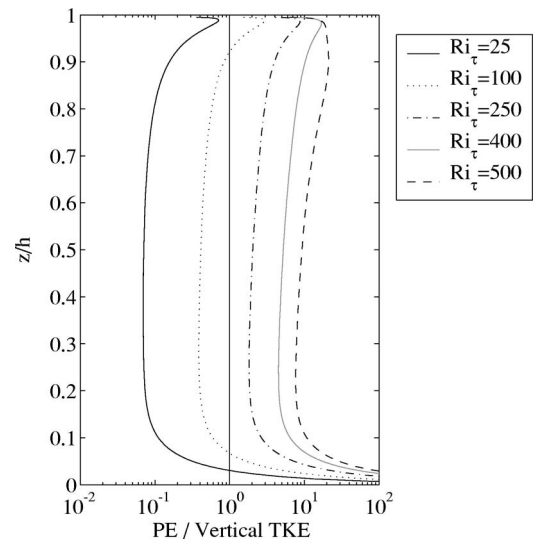
the vertical TKE, the cases with $Ri_\tau=25$ and $Ri_\tau=100$ are quite similar to the passive scalar case, $Ri_\tau=0$. The strength of the pycnocline dominates over the vertical TKE when $Ri_\tau=500$. As the low-speed fluid near the wall, on average, does not have sufficient energy to reach the surface in the latter case, a drop in $\langle u'w' \rangle$ is observed near the surface and, correspondingly, there is an increase in $\langle u \rangle$. It should be noted that, since this ratio is an *average* measure, it does not preclude the instantaneous advection of bottom fluid to the surface, but does indicate that it is much less likely when a strong pycnocline exists.

The strength and frequency of upwelling events can be quantified with a joint probability density function (PDF) of the vertical velocity, $w$, and density anomaly, $\rho'(\mathbf{x},t) = \rho(\mathbf{x},t) - \langle \rho \rangle(z)$, as shown in Fig. 16 for $Ri_\tau=0$ and 500 at $z/h=0.975$. The figure caption lists the values of $\rho'$ corresponding to the mean density at the top and bottom for comparison. The plot indicates that when $Ri_\tau=500$, it is very rare for fluid with density equal to the mean at $z=0$ (corresponding to $\rho'=0.056$ and well out of the plotted region) to be
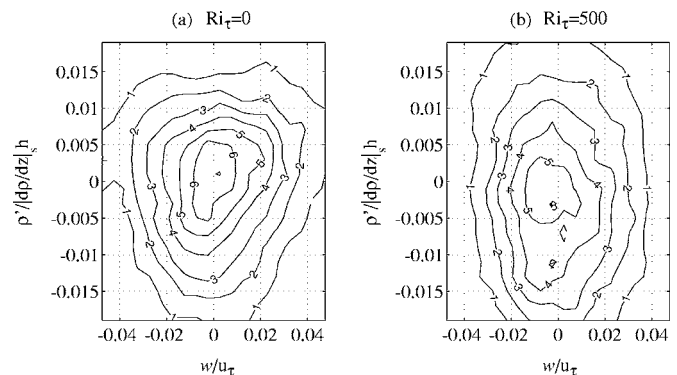


FIG. 16. Joint PDF between vertical velocity, $w$, and density anomaly, $\rho'(\mathbf{x},t) = \rho(\mathbf{x},t) - \langle \rho \rangle(z)$, at $z/h=0.975$ for (a) $Ri_\tau=0$, (b) $Ri_\tau=500$. The density anomalies corresponding to $\langle \rho \rangle$ at the top and bottom, respectively, are $-0.013$ and $0.008$ for $Ri_\tau=0$, and $-0.023$ and $0.056$ for $Ri_\tau=500$.
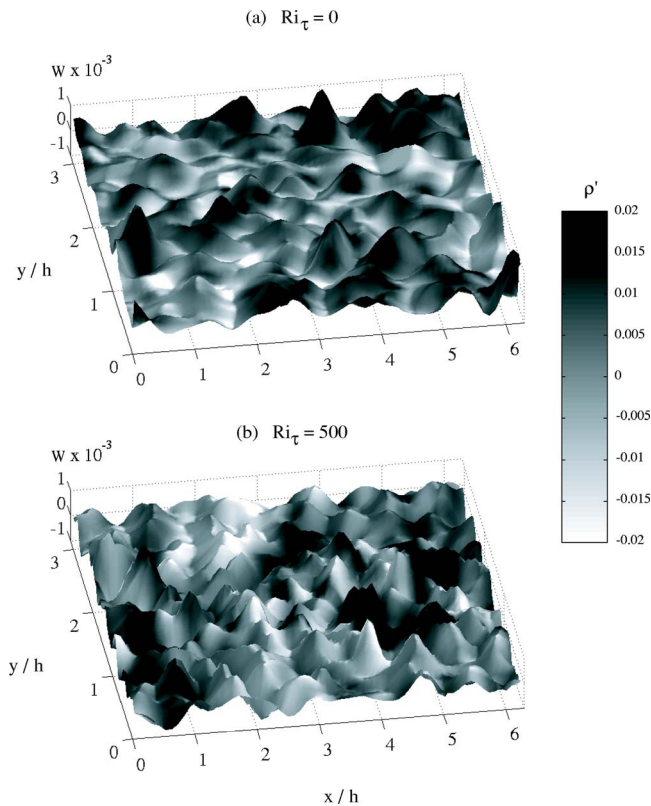
FIG. 17. Instantaneous height maps of vertical velocity with density perturbation in grayscale.



FIG. 18. (a) Ozmidov scale with Kolmogorov scale and geometric constraints, (b) ratio of Ellison to Ozmidov scales.

seen at this height. In the case of $Ri_\tau=0$ it is common to see $\rho'=0.008$, the mean at $z=0$, and the free surface value $\rho'=-0.013$ is somewhat less likely. The tails of the $w$ distribution are wider when $Ri_\tau=0$ and $\rho'>0$; a large $w$ and $\rho'>0.008$ is associated with the strong upwelling events seen when $Ri_\tau=0$ and mentioned previously. For the case of $Ri_\tau=0$, large $w$ events of both signs are associated with positive density anomaly and the distribution is nearly symmetric about $w=0$. Evidently, at this location, the downwellings of dense fluid are as strong and frequent as the upwellings. When $Ri_\tau=500$, the largest vertical velocities are no more likely to be associated preferentially with either heavy or light fluid, indicating that events with upwelling of dense fluid are not dominant.

The effect of stratification on dense fluid upwellings at the free surface can also be clearly seen by examining instantaneous visualizations of the velocity and density fields. Figure 17 shows $\rho'$ and $w'$, the deviation from the horizontal mean, at $z/h=0.999$ for $Ri_\tau=0$ and $Ri_\tau=500$ at the last simulation time in both cases. The height of the surface mesh denotes the vertical velocity with the tall peaks indicating rising fluid ($w'>0$). The corresponding grayscale shows $\rho'$ with dark gray denoting heavy fluid with positive $\rho'$. Notice that for $Ri_\tau=0$, each region of upwelling is associated with a positive density anomaly indicating an upwelling of dense fluid from the bottom. When $Ri_\tau=500$, none of the positive $w'$ patches at this particular time are associated with large positive $\rho'$. These snapshots are typical of those seen throughout the simulation; while the existence of dense fluid
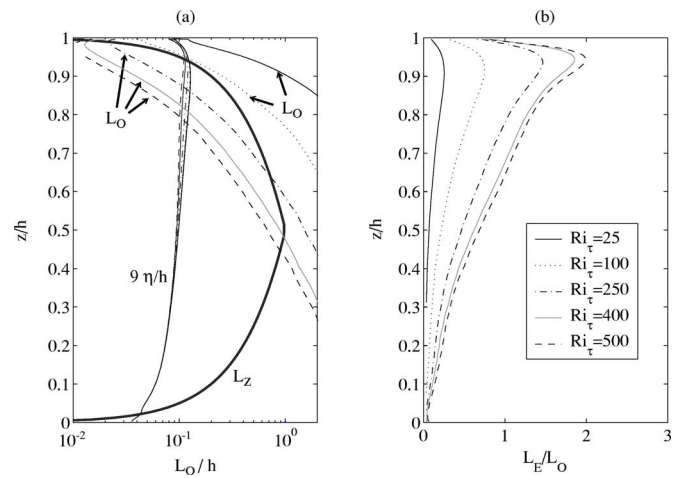
upwellings cannot be precluded for the strongest stratification cases, they are much less common than when $Ri_\tau=0$.

## D. Classification of buoyancy effects

It will be useful for the remaining discussion to precisely define regimes according to the relative influence of stratification. Since part of our flow remains unstratified, a local measure of buoyancy effects is desired. It would be possible to follow Armenio and Sarkar,[1] who, based on qualitative changes in mean flow profiles, correlation coefficients, and the buoyancy flux at $Ri_g\approx0.25$, defined a buoyancy-dominated region in the outer flow where $Ri_g(z)>0.25$, and a buoyancy-affected region near the wall where $Ri_g(z)<0.25$. From an examination of mixing diagnostics as a function of $Ri_g$ presented later in Sec. IV F, it is clear that a classification based on $Ri_g$ would not work in the present case. Instead, it is suggested that the stratification may be classified by comparing turbulent length scales with the Ozmidov scale as reported in Itsweire et al.[24] They use the Ellison length scale, $L_E$, to characterize the large scales of turbulence and the Kolmogorov scale, $\eta$, to characterize small scales, and find that the buoyancy-affected region (the beginning of departure from passive scalar behavior also called buoyancy control by these authors) begins when $L_O\approx L_E$, and buoyancy domination begins when $L_O\approx9\eta$, where $\eta$ is the Kolmogorov scale. We find that $L_E$ overestimates the large scale of turbulence and we propose that, for the bounded flow considered here, use of the distance to the nearest boundary gives a more direct estimate of the length characterizing the large vertical scales of turbulence. We define this geometric scale by $L_z=\min[2z,2(h-z)]$; the factors of 2 have been added to give a peak to crest overturning scale.

Figure 18(a) shows profiles of the Ozmidov scale along with nine times the Kolmogorov scale, and the geometric scale, $L_z$. This figure can be used to classify the relative importance of buoyancy. When $L_O>L_z$ and $>9\eta$, the departure from unstratified flow is expected to be small. When $L_O<L_z$ but $>9\eta$, the flow is buoyancy affected, and when

$L_O < 9\eta$, the flow is buoyancy dominated. It should be stressed that the demarcation between regimes is not sharp and that the definition of the length scales is only approximate. For instance, the geometric constraints on the upper and lower walls clearly should not be symmetric, and large eddies will not be isotropic. Nevertheless, the flow does appear to be qualitatively different in each regime. In particular, notice that $Ri_\tau = 25$ would be classified as unstratified, and $Ri_\tau = 100$ is only marginally buoyancy affected in the pycnocline, and we will see that these cases are qualitatively different from the others.

It is evident by reexamining the turbulent profiles that the flow behaves qualitatively different in each buoyancy regime. In each case, in the region with $L_z < L_O$, the profiles of rms velocity, Reynolds stress, and buoyancy flux collapse to the unstratified case, $Ri_\tau = 0$. For $Ri_\tau = 500$, this corresponds to $z/h < 0.4$. Note that, in this region, $N$ and $\rho_{rms}$ remain dependent on $Ri_\tau$, indicating that, although density changes remain, they are too weak for buoyancy to significantly influence the turbulence. Stratification starts to play a dynamical role in the buoyancy-affected regime when $9\eta < L_O < L_z$. This regime applies to the flow region generally below the pycnocline, and the strength of buoyancy effects additionally depends on $Ri_\tau$, e.g., the horizontal rms velocity increases and $w_{rms}$ decreases with increasing $Ri_\tau$. As will be shown, the turbulent kinetic energy budget also changes significantly with $Ri_\tau$. The location when $L_O$ becomes less than $9\eta$ roughly corresponds to the start of the pycnocline, except in the cases with $Ri_\tau = 0$ and 25 where $L_O$ is never a limiting length scale. In the buoyancy-dominated regime, the dependence of $u_{rms}$, $v_{rms}$, and $Ri_g$ on $Ri_\tau$ reverses compared to that of buoyancy-affected flow. We will see that this is also true for the mixing efficiency and the turbulent Prandtl number.

### E. Turbulent energy budgets

The profiles of the Reynolds averaged turbulent kinetic energy,

$$\langle k \rangle = \tfrac{1}{2} \langle u_i' u_i' \rangle, \tag{52}$$

are shown in Fig. 19. Several regions with distinct behavior can be identified. First, below $z/h \approx 0.4$ all cases behave like the passive scalar case, $Ri_\tau = 0$, and stratification is not felt. Then in the region $0.4 \leq z/h \leq 0.85$, the value of $\langle k \rangle$ increases with increasing $Ri_\tau$. Finally, in the near-surface region where the more stratified cases become buoyancy-dominated, the behavior is more complicated, first increasing with $Ri_\tau$ when $Ri_\tau \leq 250$ and then decreasing in the largest stratification cases.

At statistically steady state, the Reynolds averaged turbulent kinetic energy budget can be written

$$-\frac{1}{2}\frac{\partial}{\partial z}\langle w' u_i' u_i' \rangle - \frac{\partial}{\partial z}\langle w' p' \rangle + \frac{1}{Re_\tau}\frac{\partial^2 \langle k \rangle}{\partial z^2} - \langle S_{ij} \rangle \langle u_i' u_j' \rangle$$

$$-\frac{1}{Re_\tau}\left\langle \frac{\partial u_i'}{\partial x_j}\frac{\partial u_i'}{\partial x_j} \right\rangle - Ri_\tau \langle w' \rho' \rangle - \frac{\partial}{\partial z}\langle u_i' \tau_{3i} \rangle$$

$$+\left\langle \tau_{ji}\frac{\partial u_i'}{\partial x_j} \right\rangle = \frac{\partial \langle k \rangle}{\partial t} = 0, \tag{53}$$
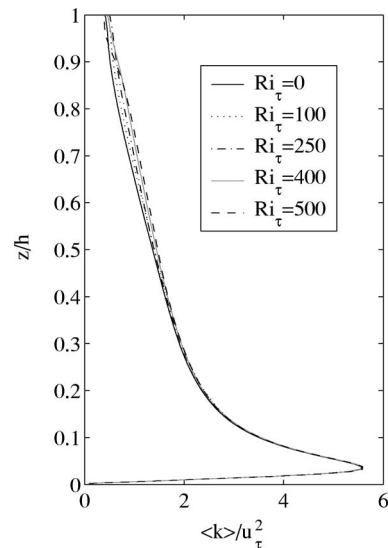


FIG. 19. Nondimensional turbulent kinetic energy.

where all terms are made nondimensional with $u_\tau$, $|d\rho/dz|_s$, and $h$. The terms are the turbulent transport, pressure transport, viscous diffusion, production, dissipation, buoyancy flux, subgrid transport, and subgrid dissipation, respectively. These terms are shown in Fig. 20 in the upper portion of the channel, and normalized by $u_\tau^4/\nu$. Near the free surface, the production decreases while the turbulent and pressure transport increase to balance the viscous loss. Such behavior is similar to that shown by Calmet and Magnaudet[25] for an LES of unstratified open channel flow at $Re_\tau = 1280$. In the lower portion of the channel, the dominant balance is between production and dissipation, and this behavior can still be seen in the lower portion of Fig. 20.

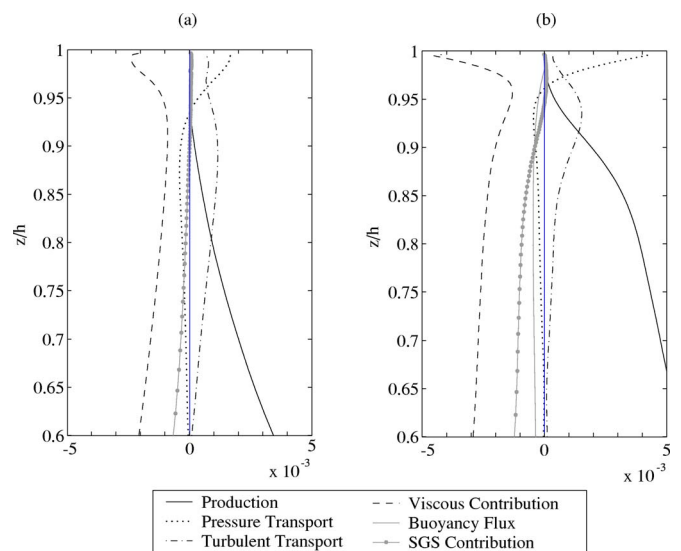The diagonal components of the pressure-strain tensor are shown in Fig. 21 where



FIG. 20. Turbulent kinetic energy budgets for (a) $Ri_\tau = 0$ and (b) $Ri_\tau = 500$, normalized by $u_\tau^4/\nu$.

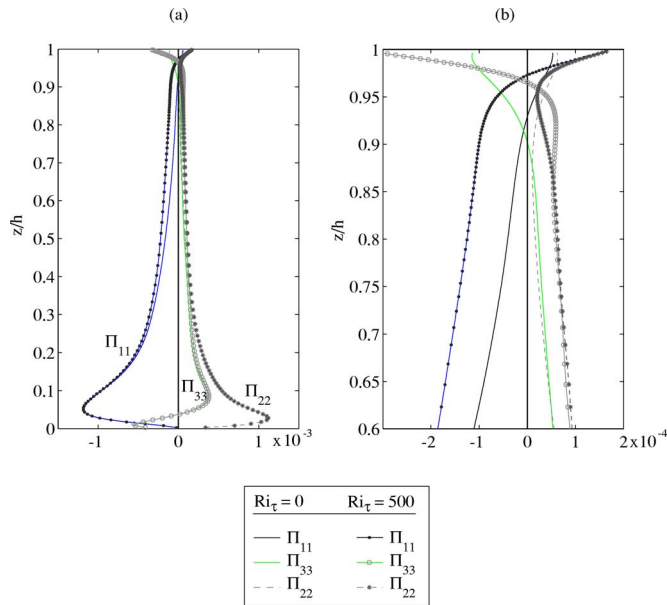(a)                                        (b)

FIG. 21. Pressure-strain correlations over (a) whole channel and (b) near-surface region. Lines denote Ri$_\tau$=0, symbols denote Ri$_\tau$=500.

$$\Pi_{ij} = \left\langle \frac{p}{\rho} \left( \frac{\partial u_i}{\partial x_j} + \frac{\partial u_j}{\partial x_i} \right) \right\rangle. \tag{54}$$

Since the trace of the tensor, $\Pi_{ii}=0$, it does not contribute to the budget for $\langle k \rangle$, but is important for the redistribution of energy among the rms velocity components. For example, as is well known and seen in Fig. 21(a), near the wall $\Pi_{11}$ is a large sink for $u_{\rm rms}$ and a source for $v_{\rm rms}$ and $w_{\rm rms}$. In this region, the pressure-strain terms act to isotropize the Reynolds stresses. This behavior holds until about $z/h=0.9$. Figure 21(b) shows the upper portion of the channel in more detail. Again, solid lines denote Ri$_\tau$=0 and lines with symbols denote Ri$_\tau$=500. In both cases, near the free surface $\Pi_{33}$ becomes negative and $\Pi_{11}$ and $\Pi_{22}$ become positive, indicating energy transfer from the wall-normal component to the horizontal directions. Since $u_{\rm rms}$ and $v_{\rm rms}$ are larger than $w_{\rm rms}$ in this area, this transfer promotes anisotropy, a behavior that has been associated with the "splatting" of fluid on the free surface.[4,7–9] Nagaosa and Saito[4] report that increasing the fixed temperature difference between the top and bottom of open channel flow decreases the transfer from vertical to spanwise directions through the pressure strain. Interestingly, here with a fixed temperature gradient at the free surface we find the opposite effect. Increasing Ri$_\tau$ increases the energy transfer from the vertical to horizontal directions. One explanation for the reduction of $\Pi_{ij}$ with increasing stratification found by Nagaosa and Saito is the partial relaminarization of the near-wall turbulence in their simulations, which results in a drop in each rms velocity component throughout the channel. The level of turbulent kinetic energy impacting the surface is therefore significantly smaller, as is the pressure-strain correlation. The effect on pressure strain in the present study need not be the same as in Nagaosa and Saito, since here the turbulent production at the lower wall is unaffected by stratification.
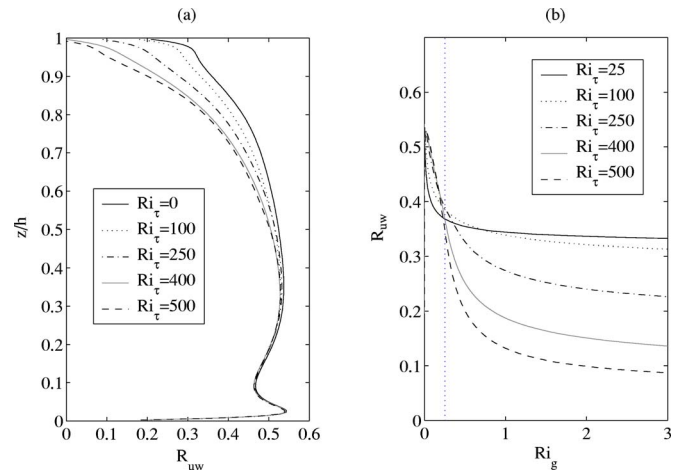


(a)                                        (b)

FIG. 22. Streamwise, wall-normal velocity correlation coefficient.

As was mentioned in Sec. I, previous studies[8,9] have shown that turbulence at a free surface without the presence of stratification cannot be well represented by two-dimensional dynamics. It is generally thought that stratification tends to make turbulence more two-dimensional, so it might be anticipated that, with sufficient stratification, the dynamics at the free surface might be approximated by a two-dimensional model. However, the turbulent kinetic energy budget at the free surface shows that vertical gradients are important. It is therefore apparent that knowledge about the subsurface three-dimensional turbulence is necessary to model the dynamics at the free surface.

Although the pressure-strain transfer from $w$ to $u$ and $v$ becomes larger with increasing Ri$_\tau$, it is interesting that the $x$-$z$ velocity correlation coefficient defined as

$$R_{uw} = - \frac{\langle u'w' \rangle}{u_{\rm rms} w_{\rm rms}} \tag{55}$$

decreases with increasing Ri$_\tau$, dropping to zero at the free surface in the case with Ri$_\tau$=500, as seen in Fig. 22(a). Our results with Ri$_\tau$=0 compare well to those of Nagaosa[9] in unstratified open channel flow, except for a few minor differences that can be explained by the fact that we use a larger friction Reynolds number, Re$_\tau$=400 compared to Re$_\tau$=150. When Ri$_\tau$=0, the value of $R_{uw}$ at the free surface is nearly half of the maximum value. However, we see that $R_{uw}$ decreases at the surface with increasing Ri$_\tau$, and when Ri$_\tau$=500, it becomes very small. When plotted as a function of Ri$_g$ as in Fig. 22(b), it appears that the behavior is well separated into two regions by Ri$_g$=0.25. When Ri$_g$<0.25, the buoyancy-affected cases (Ri$_\tau \geqslant 250$) appear to collapse to one function of Ri$_g$. For Ri$_g$>0.25, $R_{uw}$ decreases with increasing Ri$_\tau$.

### F. Mixing diagnostics

The mass flux is plotted as a function of Ri$_g$ in Fig. 23(a). The maximum occurs near Ri$_g$=0.25, and the cases with larger Ri$_\tau$ exhibit a decrease of mass flux with increasing Ri$_g$. Although this dependence on Ri$_g$ is consistent with Armenio and Sarkar,[1] it should be emphasized that there is
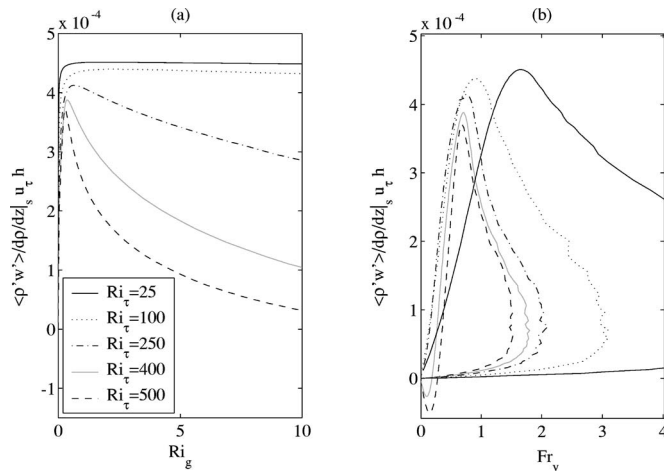
FIG. 23. Nondimensional mass flux vs (a) $Ri_g$ and (b) vertical Froude number.



FIG. 25. Mixing efficiency, $-B/(-B+\epsilon)$.

an important difference: when plotted as a function of $Ri_g$, the buoyancy flux is still strongly dependent on $Ri_\tau$. An alternate stratification parameter is the vertical Froude number,

$$Fr_v = \frac{w_{\mathrm{rms}}}{NL_E}, \qquad (56)$$

where $L_E = -\langle\rho_{\mathrm{rms}}\rangle/(d\langle\rho\rangle/dz)$ is the Ellison scale, and Fig. 23(b) gives the mass flux, replotted as a function of $Fr_v$. The three largest $Ri_\tau$ cases, where buoyancy has been seen to play an important role, show much less dependence on $Ri_\tau$ when plotted against $Fr_v$ compared to $Ri_g$. The parameter $Fr_v$ is a direct measure of the state of stratification of the turbulence itself. Collapse between cases using $Fr_v$ indicates that buoyancy affects turbulent transport, not solely the shear production as measured by $Ri_g$. The vertical Froude number has been used here instead of the isotropic turbulent Froude number, $Fr_T = (2\langle k\rangle)^{1/2}/(NL_E)$, since a better collapse of the data is obtained using only the component of the TKE directly responsible for vertical mixing. A vertical profile of $Fr_v$ in Fig. 24(a) reveals that it is largest near the bottom wall and decreases monotonically with $Ri_\tau$. At any given $z$, the
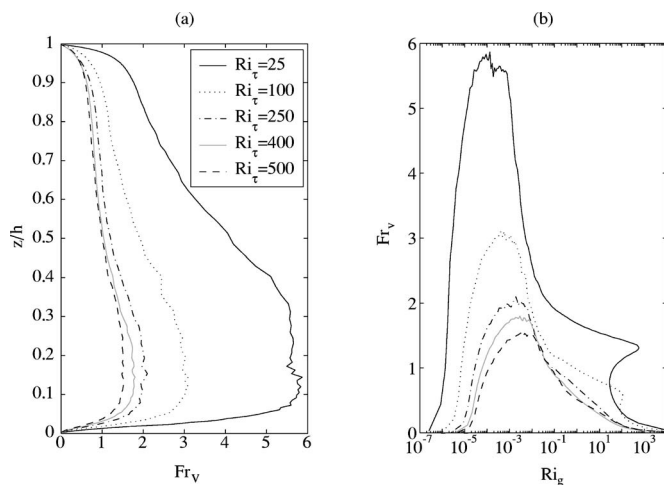


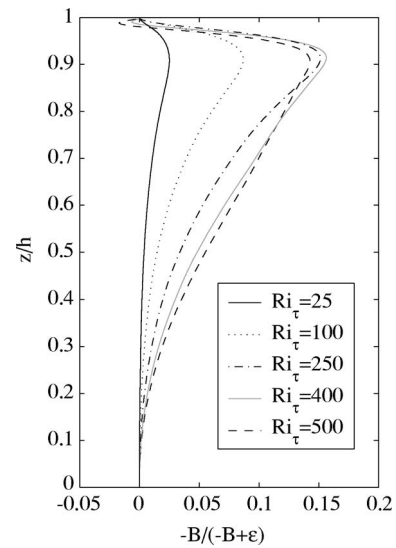FIG. 24. Vertical Froude number vs (a) $z/h$ and (b) $Ri_g$.

value of $Fr_v(z)$ decreases with increasing $Ri_\tau$, and it is this decrease in $Fr_v(z)$ between cases that is responsible in part for the observed buoyancy effects. From Fig. 24(b) it can be seen that the peak in $Fr_v$ occurs at very small $Ri_g$, about $10^{-2}-10^{-4}$, although $Fr_v$ is still $O(1)$ near the linear stability threshold, $Ri_g = 0.25$.

Ivey and Imberger[26] define a "generalized flux Richardson number,"

$$R_f = \frac{-B}{-B+\epsilon}, \qquad (57)$$

where $B = -Ri_\tau\langle\rho'w'\rangle$ is the buoyancy flux seen in Eq. (53) and $\epsilon$ is the viscous dissipation. This definition is generalized from the definition $R_f = -B/P$ to be useful for flow regions where shear production is not the dominant source of local turbulence. This quantity, limited to be between 0 and 1, is also called the mixing efficiency since it represents the ratio of the power expended in working against stratification to the total kinetic energy sink (and hence an upper limit for the energy available for mixing). This quantity is shown in Fig. 25. The maximum mixing efficiency is slightly lower than 0.2 in the highly stratified cases and does not appear to increase with $Ri_\tau$ beyond $Ri_\tau = 250$. As can be seen, the behavior is qualitatively different in the cases with smallest $Ri_\tau$. When the flow is in the buoyancy-dominated regime, the mixing efficiency appears to collapse to one function of $z/h$. Figure 26(a) shows $-B/(-B+\epsilon)$ plotted as a function of the gradient Richardson number. It is evident that even when $Ri_\tau$ and $Ri_g$ are large, the mixing efficiency is not well described by a single function of $Ri_g$. A much better collapse is obtained by plotting the mixing efficiency as a function of the vertical Froude number. As a function of $Fr_v$, the largest stratification cases collapse quite well, except perhaps when $Fr_v$ is small and the buoyancy flux becomes negative for $Ri_\tau = 400$ and 500.

The turbulent Prandtl number, defined as $Pr_T = \kappa_T/\nu_T$, where $\kappa_T$ and $\nu_T$ are the turbulent diffusivity and turbulent viscosity, respectively, is shown in Fig. 27. For $Ri_g < 0.25$,
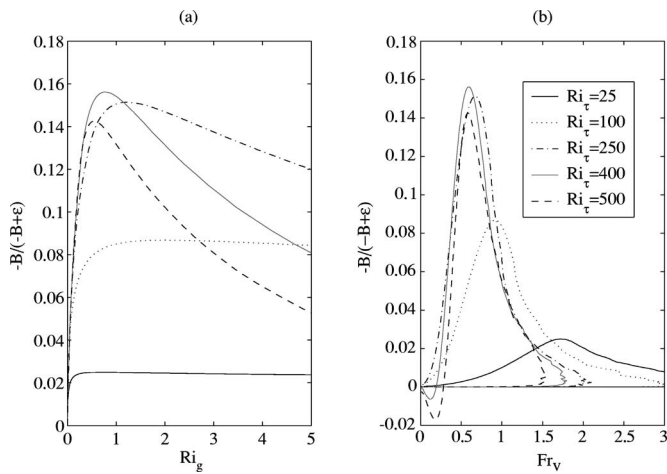
FIG. 26. Mixing efficiency, $-B/(-B+\epsilon)$, vs (a) gradient Richardson number and (b) vertical Froude number.

the value of $Pr_T$ in all cases grows rapidly with $Ri_g$, but dependence on $Ri_\tau$ is nonmonotone. For $0.25 < Ri_g < 1$, $Pr_T$ and its growth rate decrease with $Ri_\tau$. For even larger values of $Ri_g$, however, as seen in Fig. 27(b), the cases with $Ri_\tau$ $=400$ and 500 begin to grow very rapidly before $Pr_T$ becomes negative (the eddy diffusivity concept fails) when a countergradient buoyancy flux develops. This is qualitatively different from what is seen by Armenio and Sarkar[1] (see their Fig. 17). For $Ri_g < 0.2$, they report that $Pr_T \approx 1$ and is nearly constant with $Ri_g$ and $Ri_{\tau,\Delta}$. For $Ri_g > 0.2$, the less stratified cases continue growing slowly. When $Ri_\tau$ is large and $Ri_g$ $> 0.2$, they report a very rapid increase of $Pr_T$, which eventually becomes negative when countergradient buoyancy fluxes are seen. In the present study, $Pr_T$ becomes singular at much larger values of $Ri_g$. It is difficult to draw a direct comparison since Armenio and Sarkar[1] considered much larger values of $Ri_{\tau,\Delta}$ than are possible here. However, in their case 2, with $Ri_{\tau,\Delta} = 60$, they show that the buoyancy flux stays positive, and $Pr_T$ grows slowly with $Ri_g$ and does not become singular. In the present study, cases $Ri_\tau = 400$ and
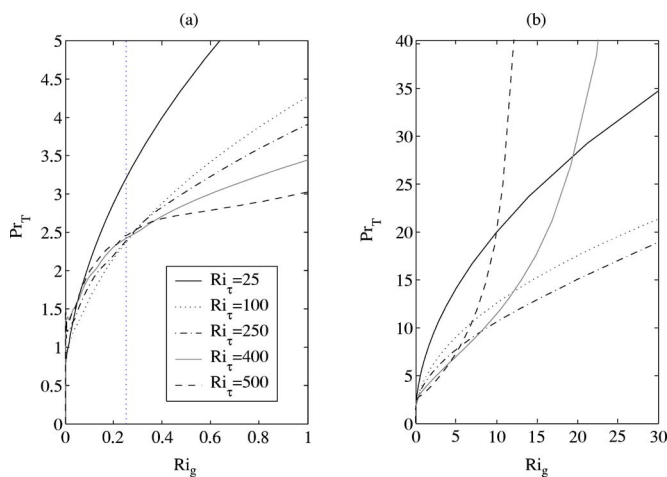
500 correspond to $Ri_{\tau,\Delta} = 24.8$ and 39.4, yet both of these cases have a countergradient buoyancy flux and a singular turbulent Prandtl number.

Buoyancy effects on mixing are sometimes ascertained by examining the ratio of the Ozmidov to Ellison scales, where the Ellison scale,

$$L_E = -\frac{\rho_{rms}}{d\langle\rho\rangle/dz}, \qquad (58)$$

is an indicator of the size of turbulent overturns. With increasing $N$, the value of $L_O$ decreases, and when $L_O$ becomes less than $L_E$, stratification is expected to become dynamically important. Note that $L_E$ is only an approximation to the turbulent overturning scale, and in particular will be an overestimate when internal waves are present and contribute to $\rho_{rms}$. The ratio of $L_E/L_O$ is shown in Fig. 18(b) as a function of $z/h$. The vertical profile maintains a similar shape, but increases in magnitude with $Ri_\tau$. The maximum value occurs just above $z/h = 0.9$ and decreases close to the free surface. $L_E/L_O$ is seen to vary significantly with $Ri_\tau$ even when plotted as a function of $Ri_g$ (not shown), and the peak value varies from about 0.25 to 2.2 at $Ri_g \approx 1$. This is contrary to the results of multiple studies of stratified shear layers where it has been observed that for $Ri_g > 0.25$, $L_E/L_O$ is maximum and remains constant with increasing $Ri_g$.[27] The behavior seen here is qualitatively different since as the free surface is approached where $Ri_g \gg 1$, $L_E/L_O$ decreases to about 1, half of its maximum value. At a given $Ri_g$, $L_E/L_O$ decreases with $Ri_\tau$. As with the mixing efficiency and the buoyancy flux, the length-scale ratio found here cannot be well described by a single function of $Ri_g$.

## G. Comparison to Armenio and Sarkar

In order to put the present results on stratification effects in perspective, it is helpful to make a brief direct comparison with the stratified channel flow simulation of Armenio and Sarkar.[1] Among the differences between the two studies are the following features of the current study: a free surface, a larger Reynolds number (increased to 400 from 180), a larger Prandtl number (5 vs 0.71), and the thermal boundary conditions (zero heat flux at the bottom and imposed heat flux at the top instead of imposed bottom and top temperatures). The primary goal of this paper is to examine how the change in thermal boundary conditions, and equivalently the manner by which stratification is imposed, affects the turbulence and its interaction with the temperature field. As was mentioned in Sec. I, this should provide some insight into the difference between an oceanic bottom boundary layer with no heat flux at the sea floor and a stable atmospheric boundary layer where the ground cools the surrounding air. While many features of a true oceanic boundary layer such as rotation, bottom roughness, and oscillatory forcing have not been considered here, any insights could be significant since the benthic boundary layer is notoriously difficult to observe in the field, and often parametrizations are developed by borrowing from knowledge of turbulence in the atmosphere.

It has been shown that the difference between the choice of boundary conditions has a very significant impact on the



FIG. 27. Turbulent Prandtl number vs $Ri_g$.

physics of the turbulence and mixing of the density field. In the present study, the near-wall region where production is large remains unstratified for all cases considered. This is also true in the benthic boundary layer where a well-mixed boundary layer of variable thickness is nearly ubiquitous.[28–30] That the dominant region of turbulence production is relatively unaffected by stratification is why the gradient Richardson number, often used in parametrizations of stratified turbulence, is less useful in the present study. Indeed, as has been shown, many turbulence and mixing quantities, when plotted as a function of $Ri_g$, do not show collapse between cases to a universal dependence on $Ri_g$ observed in previous studies of flow with vertical shear. Instead, it has been argued that stratification has an additional effect that acts to limit the vertical transport of turbulent patches by imposing a potential energy barrier. The vertical Froude number, $Fr_v$, constructed by using the vertical rms velocity and the mean density gradient, is a better indicator of such a buoyancy effect on turbulent transport and, consequently, in the upper stratified region of the channel, $Fr_v$ provides a better collapse of the mixing efficiency and buoyancy flux than $Ri_g$.

One consequence of the influence of stratification on turbulent production at the lower wall in the study by Armenio and Sarkar[1] is that the skin friction coefficient decreases sharply with $Ri_{\tau,\Delta}$, much more so than in the present study, where stratification does not significantly affect turbulent production at the lower wall. The reverse is seen, however, when considering the dependence of the buoyancy flux on $Ri_{\tau,\Delta}$. Here, the buoyancy flux becomes countergradient in the pycnocline when $Ri_\tau \geq 400$, which corresponds to $Ri_{\tau,\Delta} \geq 24.8$, while Armenio and Sarkar[1] do not observe countergradient buoyancy fluxes in the steady state until $Ri_{\tau,\Delta} = 240$. The relatively strong sensitivity of the buoyancy flux to $Ri_{\tau,\Delta}$ in the present case is likely due to the fact that nearly all of the density change across the channel occurs in the pycnocline where the countergradient buoyancy fluxes are seen. Armenio and Sarkar[1] also find the countergradient buoyancy flux near the channel centerline, but the mean density gradient is more uniformly distributed throughout the channel.

## V. CONCLUSION

Turbulent open channel flow with an imposed density gradient at the free surface corresponding to surface heating and an adiabatic bottom boundary was investigated and the effects of changing the friction Richardson number, $Ri_\tau$, have been examined. In all cases, a stably stratified pycnocline overlies a lower region that is well mixed by turbulence generated at the lower wall. As $Ri_\tau$ is increased, the turbulence in the mixed region remains unchanged while the turbulence in the pycnocline is affected by buoyancy, but never completely suppressed. It is possible that by sufficiently increasing $Ri_\tau$, the flow in the pycnocline could relaminarize, although this limit is not obtained here. It is observed that increasing $Ri_\tau$ results in an increase in the bulk Reynolds number, $Re_b$, and a deepening and strengthening of the pycnocline. The mean velocity deviates from the log law with

the extent of the deviation systematically increasing with $Ri_\tau$. Since the mean shear is too small in the pycnocline for local turbulent production, the influence of increasing the surface stratification can be explained by a potential energy barrier affecting the interaction of bottom boundary layer turbulence with the surface region. Visualizations and joint PDFs of $\rho'$ and $w$ show that upwelling of dense bottom fluid to the surface becomes rare in the large $Ri_\tau$ cases.

As has been shown in Sec. IV F, the gradient Richardson number is not enough to parametrize the buoyancy flux. Since this is contrary to some previous results, it warrants further discussion. Komori et al.[2] found that $Ri_g$ is the best parameter for describing the local effect of stratification in their heated, open channel experiments. Armenio and Sarkar[1] reach the same conclusion in a closed channel with a fixed temperature difference between the walls. The important difference between these results and the present study is that the turbulence generation region remains unstratified in our case. The boundary conditions used here separate the influence of stratification near the free surface from the flow elsewhere. The previously observed dependence on $Ri_g$, therefore, seems to be due to the stratification of the near-wall region where turbulence is produced, with this region in turn affecting the outer region. The vertical Froude number, a direct measure of the state of stratification of the turbulence, is found to be a better indicator of buoyancy effects on turbulent transport in the present configuration. Another consequence of the difference in boundary conditions is that the decrease in skin friction with increasing $\Delta\rho$ observed here is significantly smaller than that observed with constant density boundaries. Finally, we have seen that even when the density gradient becomes very large, free-surface turbulence is not well-represented by two-dimensional physics since terms involving vertical gradients remain important in the balance of turbulent kinetic energy.

[1]V. Armenio and S. Sarkar, "An investigation of stably-stratified turbulent channel flow using large eddy simulation," J. Fluid Mech. **459**, 1 (2002).
[2]S. Komori, H. Ueda, F. Ogino, and T. Mizushina, "Turbulence structures in stably stratified open-channel flow," J. Fluid Mech. **130**, 13 (1983).
[3]R. P. Garg, J. H. Ferziger, S. G. Monismith, and J. R. Koseff, "Stably stratified turbulent channel flows. I. Stratification regimes and turbulence suppression mechanism," Phys. Fluids **12**, 2569 (2000).
[4]R. Nagaosa and T. Saito, "Turbulence structure and scalar transfer in stably stratified free-surface flows," AIChE J. **43**, 2393 (1997).
[5]L. Mahrt, "Stratified atmospheric boundary layers," Boundary-Layer Meteorol. **90**, 375 (1999).
[6]R. Lien and T. B. Sanford, "Turbulence spectra and local similarity scaling

in a strongly stratified oceanic bottom boundary layer," Cont. Shelf Res. **24**, 375 (2004).

[7] R. A. Handler, J. R. Saylor, R. I. Leighton, and A. L. Rovelstad, "Transport of a passive scalar at a shear-free boundary in fully developed turbulent open channel flow," Phys. Fluids **11**, 2607 (1999).

[8] D. T. Walker, R. I. Leighton, and L. O. Garza-Rios, "Shear-free turbulence near a flat free surface," J. Fluid Mech. **320**, 19 (1996).

[9] R. Nagaosa, "Direct numerical simulation of vortex structures and turbulent scalar transfer across a free surface in fully developed turbulence," Phys. Fluids **11**, 1581 (1999).

[10] Y. Pan and S. Banerjee, "A numerical study of free-surface turbulence in channel flow," Phys. Fluids **7**, 1649 (1995).

[11] B. Perot and P. Moin, "Shear-free boundary layers: Part 1. Physical insights into near-wall turbulence," J. Fluid Mech. **195**, 199 (1995).

[12] R. J. Calhoun and R. L. Street, "Patterns on a free surface caused by underwater topography: A laboratory-scale study," Int. J. Remote Sens. **23**, 1609 (2002).

[13] J. R. Luyten, J. Pedlosky, and H. Stommel, "The ventilated thermocline," J. Phys. Oceanogr. **13**, 292 (1983).

[14] C. A. Paulson and J. J. Simpson, "The temperature difference across the cool skin of the ocean," J. Geophys. Res., C: Oceans Atmos. **86**, 1044 (1981).

[15] V. Armenio and U. Piomelli, "A Lagrangian mixed subgrid-scale model in generalized coordinates," Flow, Turbul. Combust. **65**, 51 (2000).

[16] Y. Zang, R. Street, and R. Koseff, "A non-staggered grid, fractional step method for time-dependent incompressible Navier-Stokes equations in curvilinear coordinates," J. Comput. Phys. **114**, 18 (1994).

[17] S. Komori, R. Nagaosa, Y. Murakami, S. Chiba, K. Ishii, and K. Kuwahara, "Direct numerical simulation of three-dimensional open-channel flow with zero-shear gas-liquid interface," Phys. Fluids A **5**, 115 (1993).

[18] L. Shen and D. Yue, "Large-eddy simulation of free-surface turbulence," J. Fluid Mech. **440**, 75 (2001).

[19] M. V. Salvetti and S. Banerjee, "A priori tests of a new dynamic subgrid-scale model for finite-difference large-eddy simulations," Phys. Fluids **7**, 2831 (1995).

[20] G. K. Batchelor, *The Theory of Homogeneous Turbulence* (Cambridge University Press, London, 1959).

[21] C. A. J. Fletcher, *Computational Techniques for Fluid Dynamics* (Springer, New York, 1991), Vol. 2.

[22] S. B. Pope, *Turbulent Flows* (Cambridge University Press, Cambridge, 2000).

[23] A. E. Gill, *Atmosphere-Ocean Dynamics* (Academic, New York, 1982).

[24] E. C. Itsweire, J. R. Koseff, D. A. Briggs, and J. H. Ferziger, "Turbulence in stratified shear flows: Implications for interpreting shear-induced mixing in the ocean," J. Phys. Oceanogr. **23**, 1508 (1993).

[25] I. Calmet and J. Magnaudet, "Statistical structure of high Reynolds-number turbulence close to the free surface of an open-channel flow," J. Fluid Mech. **474**, 355 (2003).

[26] G. N. Ivey and J. Imberger, "On the nature of turbulence in a stratified fluid. Part I: The energetics of mixing," J. Phys. Oceanogr. **21**, 650 (1991).

[27] U. Schumann and T. Gerz, "Turbulent mixing in stably stratified shear flows," J. Appl. Meteorol. **34**, 33 (1995).

[28] L. Armi and R. C. Millard, "Bottom boundary-layer of the deep ocean," J. Geophys. Res. **81**, 4983 (1976).

[29] E. D'Asaro, "Velocity structure of the benthic ocean," J. Phys. Oceanogr. **12**, 313 (1982).

[30] C. Garrett, P. MacCready, and P. Rhines, "Boundary mixing and arrested Ekman layers: Rotating stratified flow near a sloping boundary," Annu. Rev. Fluid Mech. **25**, 291 (1993).